공학박사 학위논문

Applications of novel thin-film deposition techniques to organic solar cells: Low-temperature aqueous deposition of ZnO and thin-film transfer of polymer:fullerene films

새로운 박막 증착 기술의 활용을 통한 유기 태양전지의 제작:
ZnO 박막의 저온 수용액 증착법 및 고분자:풀러렌 박막 전사법

2019년 8월

서울대학교 융합과학기술대학원

융합과학부 나노융합전공

가 윤 석

Applications of novel thin-film deposition techniques to organic solar cells: Low-temperature aqueous deposition of ZnO and thin-film transfer of polymer:fullerene films

지도 교수 : 김 창 순

이 논문을 공학박사 학위논문으로 제출함
2019년 7월

서울대학교 융합과학기술대학원
나노융합학과
가 윤 석

가 윤 석의 공학박사 학위논문을 인준함
2019년 6월

위 원 장	김 연 상	(인)
부위원장	김 창 순	(인)
위 원	송 윤 규	(인)
위 원	이 강 원	(인)
위 원	이 정 용	(인)

Abstract

Applications of novel thin-film deposition techniques to organic solar cells: Low-temperature aqueous deposition of ZnO and thin-film transfer of polymer:fullerene films

Yoonseok Ka

Program in Nano Science and Technology

Graduate School of Convergence Science & Technology

Seoul National University

In the field of organic solar cells, researchers are most interested in commercializing organic solar cells through the implementation of flexible devices and the fabrication of high-efficiency devices comparable to silicon-based solar cells. Flexible solar cells and high-efficiency organic solar cells must be accompanied by the design freedom of the device to enable them. The

problem of hindering the degree of freedom of device design mainly occurs in the process of forming a thin-film using a solution process. Problems that occur during the thin-film deposition through the solution process can be summarized as follows. First, damage of underlying organic layer(s) and plastic substrate by high annealing temperature during the thin-film deposition process. Second, damage of organic layer(s) by organic solvents during the thin-film deposition process. Therefore, development of thin-film deposition technique for a low-temperature solution process and development of a thin-film deposition technique that can prevent the damage of the organic layer(s) by organic solvents are essential elements for realizing a high-efficiency and commercialization devices.

In this thesis, I describe the research that can expand the design freedom of organic solar cells by developing solution-based novel thin-film deposition techniques. First, a ZnO thin-film deposition method using an aqueous ammine-hydroxo complex, which is a deposition method of an electron transport layer capable of a low-temperature solution process, is introduced for flexible device fabrication. Moreover, it is applied to the inverted polymer solar cells to exhibit that it is possible to fabricate the device with high performance even at a process temperature as low as 80 ºC. Also, the effects of annealing temperature on the properties of thin-films during the ZnO thin-film deposition process were investigated by XPS, UPS, GI-WAXS, and

optical transmittance measurements.

Next, to solve the damage problem of the organic layer(s) by the organic solvents, the polymer:fullerene thin-film transfer technique using PDMS stamps was developed to fabricate the organic tandem solar cells. Through the thin-film transfer technique, the degree of freedom of arrangement of the small molecule- and polymer- absorption layer of hybrid organic solar cells is expanded. As a result, it is possible to efficiently arrange the absorption layers only taking into account the complementary absorption spectra. The hybrid organic tandem solar cell thus produced achieved the power conversion efficiency of 6.26%.

Last, the thin-film transfer technique was applied to polymer tandem solar cells. I applied small-molecule based ICL formed by vacuum evaporation to polymer tandem solar cells. By using dry thin film transfer technique, a polymer layer was formed without damaging the underlying organic layer(s) to overcome the restriction of ICL material selection in polymer tandem solar cells. Based on the results of this study, the flexibility of material selection for the development of ICL of polymer tandem solar cells connecting the top and bottom subcells without an electrical and optical loss was greatly improved.

Keywords: Organic electronics, solar cell, tandem, transfer, thin-film, small molecule, polymer, interconnection layer

Student Number: 2011-22751

Table of contents

List of figures

with a $J_{SC} = \text{Max}(J_{SC1}, J_{SC2})$.

Figure 1.8 Simplified schematic band diagram of tandem solar cells. (a) conventional structure. (b) inverted structure.

Figure 2.1 Common ZnO thin-film deposition methods. a) Sol−gel based ZnO thin-film deposition method. b) ZnO nanoparticle method.

Figure 2.2 Current density–voltage characteristics of inverted polymer solar cells (IPSCs) with a ZnO electron transport layer (ETL) under simulated 1 sun AM1.5G illumination. The ZnO ETLs were deposited by spin coating an aqueous solution of an ammine-hydroxo zinc complex, followed by thermal annealing at different temperatures. Inset: Structure of the IPSCs.

Figure 2.3 Current density – voltage characteristics of inverted polymer solar cells with a ZnO electron transport layer in the dark.

Figure 2.4 O 1s XPS spectra of ZnO films on ITO-coated glass substrates, annealed at 25 °C (filled squares), 60 °C (open squares), 90 °C (filled circles), and 150 °C (open circles). Solid lines are fits to the experimental data by two Gaussian functions centered at 530.9 ± 0.1 eV and 532.5 ± 0.4 eV.

Figure 2.5 Grazing incidence wide-angle X-ray scattering patterns of the ZnO films on ITO-coated glass substrates. The patterns were vertically displaced for clarity, and the pattern for an ITO-coated glass substrate without a ZnO film was reduced by a factor of three.

Figure 3.5 Schematic illustration of fabrication of hybrid organic tandem solar cells by the thin-film transfer technique. (a) Spin-coating of a PCPDTBT:$PC_{70}BM$ solution on a PDMS stamp and removal of a solvent and an additive. (b) Bottom subcell deposition on an ITO-coated glass substrate by thermal evaporation in vacuum. (c) Pressing of the stamp on the substrate with mild heating. (d) Peeling off the PDMS stamp from the substrate. (e) Deposition of the top electrodes.

Figure 3.6 Current density vs voltage (*J–V*) characteristics of single-junction and tandem solar cells. (a) *J–V* characteristics of transfer-fabricated organic tandem solar cells with varying TAPC:C_{70} thickness. (b) *J–V* characteristics of transfer-fabricated and spin-coated tandem cells with 120-nm-thick TAPC:C_{70} layers, and two single-junction cells whose active layers are TAPC:C_{70} and PCPDTBT:$PC_{70}BM$, respectively.

Figure 3.7 Cross-sectional transmission electron microscope (TEM) images of hybrid organic tandem solar cells. Cross-sectional TEM image of (a) spin-coated and (b–d) transfer-fabricated tandem solar cells. (c) and (d) are the images of the regions enclosed by black and red squares in (b), respectively. For the transfer-fabricated device, thicknesses of the transferred PCPDTBT:$PC_{70}BM$ layer (i) and the thermally evaporated small-molecule layers (ii) were unchanged from the designed values. The features (iii) and (iv) in (d) were generated during focused-ion beam milling used in sample preparation.

Figure 3.8 Calculated and measured short-circuit current densities (J_{SC}) of the

transfer-fabricated tandem devices with different TAPC:C_{70} thicknesses (t). The calculated (line) and measured (circle) values of J_{SC} for the transfer-fabricated tandem device shown in Fig. 3.3 as functions of t. The inset shows the photocurrent densities of the top (solid line) and bottom (dotted line) subcells as functions of t.

Figure 4.1 (a) Structure of the polymer tandem solar cells device fabricated using a thin-film transfer technique, and chemical structure of photoactive materials. (b) Spectra of the absorption efficiencies of the top (red) and bottom (blue) active layers calculated using the transfer matrix method. Also shown is the calculated absorption efficiency spectrum of the tandem device as a whole (green), compared with that measured for the tandem device fabricated using the thin-film transfer technique (black).

Figure 4.2 Transmittance spectrum of interconnection layer of tandem device composed of 10 nm BCP:Ag / 0.5 nm Ag island / 10 nm HAT-CN.

Figure 4.3 (a) Deposition of a HAT-CN layer on a UV-ozone treated ITO substrate. (b) Transfer of a P3HT:PC_{60}BM film from a stamp to the HAT-CN layer. (c) Peeling off the stamp from the substrate. (d) Deposition of an ICL onto the bottom subcell using thermal evaporation in a vacuum. (e) Transfer of a PCPDTBT:PC_{70}BM layer onto the ICL. (f) Deposition of the top electrodes.

Figure 4.4 Photovoltaic characteristics of polymer tandem solar cells using an ICL with varying thicknesses of BCP:Ag layer and Ag islands ($t_{BCP:Ag}$ and t_{Ag},

respectively). (a) *J–V* characteristics of the tandem cells with t_{Ag} = 0.5 nm and different $t_{BCP:Ag}$ values. (b) *J–V* characteristics of the tandem cells with $t_{BCP:Ag}$ = 10 nm and different t_{Ag} values. (c) Photovoltaic parameters of the tandem cells as functions of $t_{BCP:Ag}$ and t_{Ag}. (d) *J–V* characteristics of the tandem device with $t_{BCP:Ag}$ = 10 nm and t_{Ag} = 0.5 nm, compared with the characteristics of the single junction devices. Inset: photovoltaic parameters of the three devices.

Figure 4.5 External quantum efficiency (EQE) spectra of the tandem device with $t_{BCP:Ag}$ = 10 nm and t_{Ag} = 0.5 nm measured under light biases at 532 nm (red) and 680 nm (black) show a qualitative agreement with the calculated absorption spectra of the subcells shown in Fig. 4.1b. The EQE measurements were performed by following a method described elsewhere. A monochromatic light generated using a laser-driven light source (EQ-99, Energetiq) and a monochromator (Monora 200, Dongwoo Optron) was modulated by a chopper at a frequency of ~400 Hz before irradiating the device, and the resulting photocurrent was measured using a current amplifier (SR570, Stanford Research) and a lock-in amplifier (SR830, Stanford Research).

Figure 4.6 Photovoltaic parameters extracted from intermittently measured *J–V* characteristics of the optimized tandem cell. The measurement was performed without encapsulation in ambient at 50 % relative humidity.

Figure 4.7 (a) Device-to-device variations of the *J–V* characteristics of the tandem cells shown in Fig. 4.4b. Top and bottom of errors bars correspond to maximum and minimum values obtained from eight devices for each tandem cell. (b) The

List of tables

Chapter 1 Introduction

1.1 General introduction

1.1.1 Introduction to organic solar cells

The organic solar cell is a renewable energy device in which an organic material-based light-absorbing layer absorbs photons to generate electric energy. Types of organic solar cells can be divided into fabrication technology, material characteristics, and device design. Two main fabrication technologies can be distinguished by wet processes or thermal evaporation. Depending on the difference in device structure, the device can be classified into a single layer, a bilayer heterojunction, and a device having a bulk heterojunction. The single layer device is composed of only one active material, while the other structure relates to each of the two kinds of materials, electron donor (D) and electron acceptor (A). The difference of these architectures is in the charge generation mechanism. Single-layer devices typically require a Schottky barrier at one contact, so that exciton separation occurs at this barrier. D−A solar cells apply photo-induced electron transfer to separate electrons from holes. The photo-induced electron transfer occurs from the lowest unoccupied molecular orbital (LUMO) of donor to the LUMO of the acceptor, and therefore must be a good electron acceptor with strong electron affinity. The separated electrons and holes transport to the anode and the cathode of the

device, respectively.

1.1.2 Characterization of organic solar cells

The power conversion efficiency (PCE) that represent the performance of organic solar cells is determined from equation (1).

$$\mathrm{PCE} = \frac{V_{OC} \times J_{SC} \times FF}{P_{in}} \quad (1)$$

The P_{in} is the incident solar power, typically 100 mW/cm^2. The short circuit current density (J_{SC}) is the maximum photocurrent generation value. It corresponds to the y-intercept value of standard current−voltage curve (Fig. 1.1). The open circuit voltage (V_{OC}) is the voltage when J_{SC} is zero. Within bulk heterojunction organic solar cells, this value is highly dependent on the highest occupied molecular orbital (HOMO) and LUMO energy levels and work functions for the light-absorbing materials. The fill factor (FF) is the quotient of the maximum power value and the product of the V_{OC} and short circuit current. The FF is essentially a measure of how efficiently generated charges are extracted from the device. This can be thought of as a competition between charges transporting through the whole device, and charges that recombine.

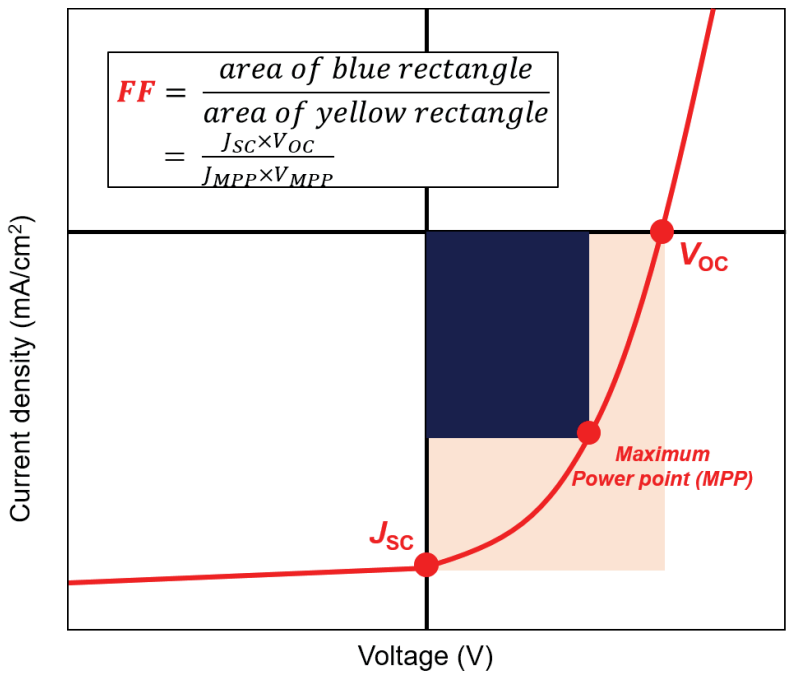

Figure 1.1 Standard current density – voltage curve of organic solar cell and its photovoltaic factors. J_{SC}, V_{OC}, and FF.

1.1.3 Working principle of D−A heterojunction solar cells

The process by which D–A heterojunction solar cells generate photocurrent (Fig. 1.2) can be explained by the following procedure. (1) The photons incident in the solar cell are absorbed by the donor. The absorption efficiency at this time is η_{PA}, which depends on the types and thickness of the materials. (2) The donor absorbs photons to form excitons, and the formed excitons migrate to the interface between donor and acceptor with the probability of η_{ED}. (3) The exciton moving to the interface moves to charge transfer (CT) or charge separated state by the energetic driving force, and the probability of this process is called η_{CT}. (4) The process of separating the electron-hole pairs of the CT state into electrons and holes is called charge dissociation. The probability of this process occurring is called η_{CD}. (5) The electrons and holes thus separated travel to the cathode and the anode, respectively, and the charge transport efficiency (η_{CP}) is defined as the probability of the electrons and holes moving without being lost through recombination. (6) Finally, the probability that electrons and holes moved to the electrode are extracted to each electrode is called charge collection efficiency (η_{CC}). This is only a direct loss path for particles if contacts are not selective and a charge carrier reaches the wrong contact, where it is extracted. Selective contacts inhibit this particle loss, and consequently η_{CC} is "1". The external quantum efficiency (EQE) as

a function of wavelength, applied bias V and temperature is a product of the single efficiency:

$$\mathrm{EQE}\ (\lambda, \mathrm{V}, \mathrm{T}) = \eta_{PA}(\lambda) \cdot IQE(\lambda, V, T)$$

$$= \eta_{PA}(\lambda)\eta_{ED}(T)\eta_{CT}(T)\eta_{CD}(V,T)\eta_{CP}(V,T)\eta_{CC}(V,T) \qquad (2)$$

In summary, EQE can be expressed as the product of η_{PA} and internal quantum efficiency (IQE), and IQE is an electrical process in the device, which is the efficiency of how efficiently the absorbed photons are separated into the electrons and holes.

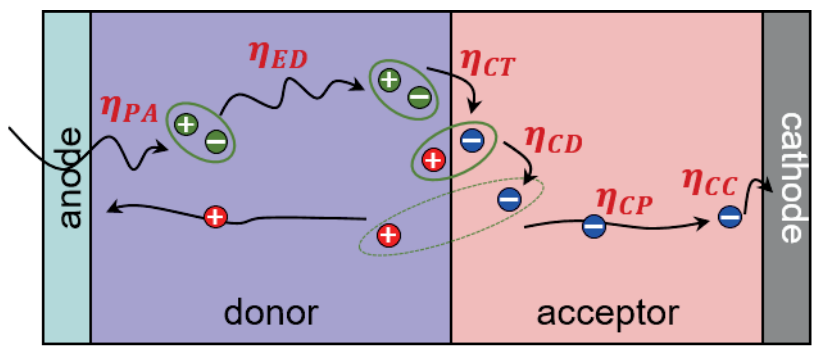

Figure 1.2 Schematic diagram of photocurrent generation process in D–A heterojunction solar cell.

1.1.4 Challenges for making organic solar cells competitive

These organic solar cells have differentiated characteristics from inorganic solar cells in the following points. It is advantageous in that it is lightweight, thin, and transparent and can be fabricated on a flexible substrate. Because of these advantages, it is possible to fabricate transparent devices or colorful devices, and thus it can be installed in a glass window of a building or has a possibility of being used as a wearable device. However, in order to commercialize organic solar cells, the following two problems must be solved. First, the development of low-temperature thin-film deposition technique for flexible device fabrication. Second, the implementation of devices that can overcome low power conversion efficiency compared to inorganic solar cells.

In order to realize a flexible device, a plastic substrate having a low glass transition temperature ($\leq$ 100 ºC) should not be damaged during fabrication of the device. Therefore, the entire layers must be deposited at a low temperature of 100 ºC or less. The biggest problem to solve for this is to form the metal oxide layer, which requires a high annealing temperature at low-temperature. The development of a technique for depositing a high-quality metal oxide thin-film at a low temperature enables the realization of flexible organic solar cells, which are meaningful research that can advance the commercialization of the organic solar cells.

To increase the efficiency of organic solar cells, they must absorb more photons and convert them into charges efficiently. The following approaches are available for the efficient absorption of photons. First, low-bandgap light-absorbing materials must be developed to absorb a wide range of light, including wavelengths that are not used efficiently (700 to 900 nm) [1−3]. The absorption mechanism of the photons using the low band gap absorption layer is as follows (Fig. 1.3a). (I) photons having different wavelengths are incident on the low band gap absorption layer. (II) Among them, photons having energy larger than the band gap energy (E_g) of the absorption layer are absorbed. In this process, the difference between the E_g and the photon energy is lost as heat (curly red arrow) [4]. (III) On the other hand, photons having energy smaller than E_g are transmitted to the absorbing layer without being absorbed. Next, the absorption efficiency can be improved by increasing the thickness of the light-absorbing layer. In this case, there is a limit to the increase in the thickness of the light-absorbing layer due to the limitations of the organic material having low carrier mobility and a short exciton diffusion length [5−7].

To overcome these problems, an organic tandem solar cell (OTSC) has been developed that efficiently absorbs photons by stacking absorbing layers with complementary absorption spectra using the interconnection layer (ICL,

blue layers as shown in Fig. 1.3b). Accordingly, the tandem solar cell efficiently absorbs a wide range of light, thereby enabling it to overcome low efficiency, which is a disadvantage of organic solar cells. The photon absorption mechanism of the tandem device is as follows (Fig. 1.3b). (I) photons having different energies are incident on the stacked absorbing layers (E_{g1}, E_{g2}, E_{g3}). (II) Photons having energy smaller than the band gap energy (E_{g1}) of the absorption layer are transmitted, and photons having energy larger than E_{g1} are absorbed at that absorbing layer. (III) Among photons transmitted through the same procedure, photons having energy larger than E_{g2} are absorbed in the second absorption layer, and photons having energy smaller than that are transmitted and absorbed in the absorption layer having the band gap energy of E_{g3}, thereby minimizing energy loss due to heat.

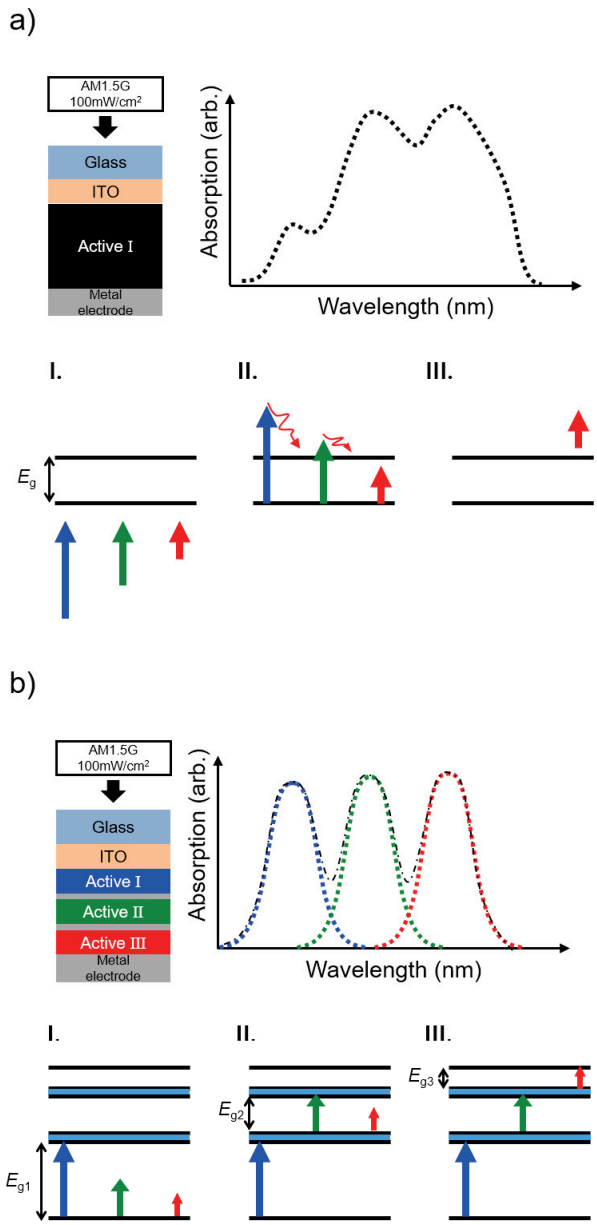

Figure 1.3 (a) Photon absorption mechanism in a solar cell with single-junction solar cell. (b) photon absorption mechanism in a multi-junction solar cell.

1.2 Conventional solution-based method for metal oxide thin-films deposition

1.2.1 Sol–gel methods

The sol–gel method is the most widely known metal oxide thin-film deposition method. Since the synthesis of silica gel by Ebelman in 1846 [8], this method has been developed progressively and sol–gel synthesized materials have been implemented in several applications with excellent optical, electrical, thermal and mechanical properties. Thin-films and various shapes of metal nanoparticles can be formed by the sol–gel method. The soles can be deposited onto the substrates as thin-films using these techniques; (1) spin-coating and (2) dip coating. The gelation process is done condensation of the sol or addition of the polymer. After that, high-temperature heat treatment must be performed to form a thin-film and to form particles having various shapes.

1.2.2 Nanoparticle deposition methods

A metal oxide nanoparticle deposition method which forms a thin-film using a solution prepared by synthesizing metal oxide nanoparticles of a desired shape and size is another well-known type of metal oxide thin-film deposition method. Unlike the sol–gel method, the nanoparticle method is advantageous in that it does not require high-temperature heat treatment after coating the

nanoparticles because the thin-film is deposited using the metal oxide nanoparticles already formed. However, it is a disadvantage of the nanoparticle method that it is necessary to form a thick-film for good quality film without pin-holes and to remove the ligands used for nanoparticle dispersion. When a thick metal oxide film is applied to a device, it acts as a large resistance, and a pinhole-rich film causes leakage current of the organic solar cells.

1.3 Types and working mechanisms of organic tandem solar cells

1.3.1 Types of organic tandem solar cells

1.3.1.1 Small-molecule tandem solar cell

The small-molecule tandem solar cell (STSC) has small-molecular absorbing layers that are formed through thermal evaporation in vacuum. Therefore, it has advantages when forming multiple layers, having cascade structures as well as control over conductivity and mobility that are achieved through precise thickness control and the doping of each layer.

Much research has been conducted on the development of STSCs based on the advantages of the easy construction of multiple layers using various kinds of materials. Since the first report of the STSCs by *Hiramoto et al*. in 1990 [9], we have made much progress and reported the results of the study

on the fabrication of STSCs (Fig. 1.4a). In 2002, Forrest group demonstrated high open-circuit voltage (V_{OC}) STSCs that incorporated dual, triple, and fivefold heterojunction consisting of CuPC and PTCBI as a donor and an acceptor, respectively (Fig. 1.4b) [10].

STSCs composed of various kinds of ICLs and light-absorbing layers have been developed since many materials can be readily arranged through vacuum thermal deposition, and it is easy to form a multilayer-structured ICL. As a result, the maximum power conversion efficiency(PCE) has increased to 12%, which was recently reported by Heliatek [11].

1.3.1.2 Polymer tandem solar cells

The polymer tandem solar cell (PTSC) has the bulk-heterojunction consisting of a polymer donor and a fullerene derivative acceptor as light-absorbing layers. Unlike the STSCs, it is possible to mass produce PTSCs at low cost through the application of large area process because the thin-film can be formed through the solution process.

The first PTSC was reported in 2006 by Kawano et al. [12]. Using a poly[2-methoxy-5-(3′, 7′-dimethyloctyloxy)-1,4-phenylenevinylene] (MDMP -PPV) donor and a fullerene derivative blend of $PC_{60}BM$ acceptor as the light-absorbing layer, this device achieved a PCE of 3.1%. The device was fabricated by stacking two identical absorbing layers, which resulted in a 35%

improvement in efficiency compared to a single device. In the first PTSCs, the deposited metal clusters were used as the ICL, resulting in a V_{OC} loss. Later, an ICL consisting of a junction of p- and n-doped transport layers was introduced, which significantly improved V_{OC} loss. The first all-solution process PTSC was developed in 2007 by Gilot et al. [13] and Kim et al. [14]. These devices used ICLs consisting of a hole transport layer (HTL) of PEDOT:PSS and an electron transport layer (ETL) of ZnO or TiO_x. Also, in the latter case, a PCE of 6.5% was achieved (Fig. 1.5a). Since then, PTSCs have been steadily increasing their efficiency with the development of light-absorbing materials. Through the development of light-absorbing materials with complementary absorption spectra, Meng et al. successfully developed PTSCs with the highest PCE of 17.36% (Fig. 1.5b) [15]. As such, PTSCs can be applied to processes that can be mass-produced and are being commercialized through the development of light-absorbing materials.

However, despite these advances, the efficiency of PTSCs is still below that of inorganic-based solar cells, and the following limitations must be solved for commercialization. First, it is necessary to develop high-efficiency low-bandgap materials that can minimize the spectrum overlap with the high-bandgap materials. Next, the development of process techniques capable of efficiently arranging such light-absorbing layers and the development of

various kinds of ICLs are required. If these problems are solved, it is possible to fabricate a highly efficient OTSC that is theoretically close to 30% so that it can be brought closer to commercialization.

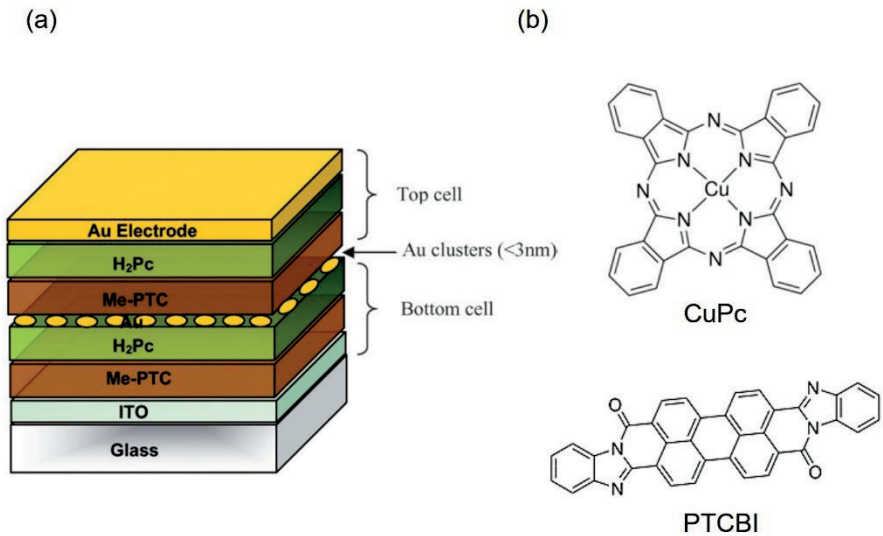

Figure 1.4 (a) Structure of the first report of the small-molecule tandem solar cell [9] Reprinted with permission of Chem. letter. (b) molecular structure of materials composing the light-absorbing layer of small-molecule tandem solar cell reported by Forrest group [10]. Reprinted with the permission of AIP Publishing.

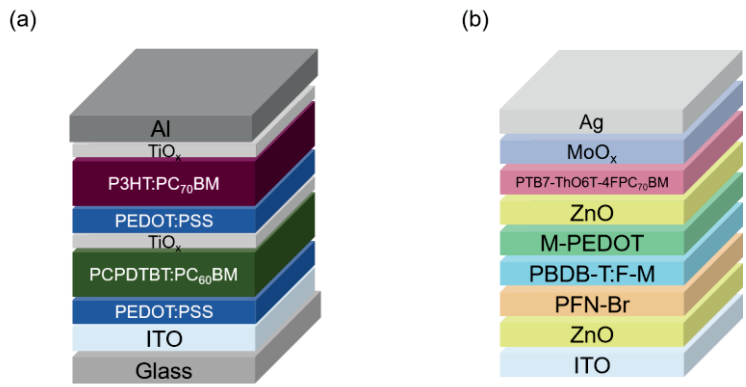

Figure 1.5 (a) Structure of the first reported all-solution process polymer tandem solar cell [14]. (b) structure of the polymer tandem solar cell with the highest efficiency reported to date [15].

1.3.2 Working mechanism of the organic tandem solar cells

1.3.2.1 Material selection of absorption layers and their arrangement

The absorbing layers of the OTSC consist of a high-bandgap absorbing layer that absorbs photons in a short wavelength region and a low-bandgap absorbing-layer that absorbs photons in a long wavelength region. In order for the OTSC to efficiently absorb photons, it is necessary to arrange absorption layer materials in consideration of optical interference. Therefore, the arrangement of the high-bandgap material and the low-bandgap material (Fig. 1.6a) and the arrangement of the small-molecule- and polymer-based light absorbing materials (Fig. 1.6b) should be made to absorb photons efficiently. In the case of a tandem solar cell connected in series, the ideal V_{OC} of a tandem device is represented by the sum of the V_{OC} of each subcell constituting the tandem device as denoted in equation (1). However, the J_{SC} of the tandem device is determined for each subcell combination. It entirely depends on the FF of each subcell. The J_{SC} of a tandem device consisting of a subcell having a lower J_{SC} and significantly higher FF and a subcell having a higher J_{SC} and extremely low FF is determined as J_{SC} = Min(J_{SC1}, J_{SC2}) according to Kirchhoff's law (Fig. 1.7a). On the other hand, the J_{SC} of a tandem device consisting of a subcell with extremely low FF and lower J_{SC} and a subcell with very good FF and higher J_{SC} is determined as J_{SC} = Max(J_{SC1}, J_{SC2}) (Fig. 1.7b)

[16].

$$V_{OC-series\ tandem} = V_{OC-bottom} + V_{OC-top} \quad (1)$$

Therefore, in order for the tandem device to have the maximum J_{SC}, each subcell constituting the device must exhibit a high J_{SC} and a high FF, so that it is necessary to have a structure capable of minimizing the spectrum overlap of each absorbing layer and readily transporting the charge. However, in the case of the bottom subcell of the tandem device, the J_{SC} reduction occurs due to the absence of mirror reflection. Also, in the case of the top subcell, the J_{SC} loss occurs as the absorption in the short wavelength region due to the overlap of fullerene or fullerene derivatives used as the acceptor of each subcell decreases. Recently, organic solar cells using non-fullerene acceptor have been developed to overcome these limitations and produce tandem solar cells with higher efficiency [17−19].

The transfer of charges generated in the bottom and top light-absorbing layers of the OTSC can be explained by the simplified band diagram schematically shown in Fig. 1.8. In the conventional(/inverted) tandem device, the bottom transparent electrode, ITO, serves as the anode(/cathode). The holes(/electrons) generated from the bottom light-absorbing layer are transported to the ITO electrode, and the electrons(/holes) move to the recombination site through the ETL(/HTL). At the same time, the

electrons(/holes) generated from the top light-absorbing layer are transported to the top metal electrode, and the holes(/electrons) move to the recombination site through the HTL(/ETL) and recombine with electrons(/holes) injected from the bottom light-absorbing layer.

1.3.2.2 The interconnection layers for organic tandem solar cells

The structure of the ICL, which is one of the essential components of the OTSC, can be classified as follows. First, it is a structure composed of a p-type material with a high work-function and an n-type material with a low work-function. Second, it is a structure consisting of a thin metal film or metal clusters. Third, it is a structure consisting of a doped p-n junction. Last, it is a structure in which metal is inserted between p-type and n-type materials. The ICL of the tandem device having these structures is a factor that significantly affects the operation of the tandem device which has to play a role to induce the facile recombination of electrons and holes injected from the top and bottom subcells.

The conditions that the ICL of the OTSC should satisfy are as follows. First, the ICL should connect each subcell electrically without voltage loss. Second, the ICL must have high transmittance in the visible region to minimize the optical loss. Third, the quasi-Fermi level of the electrons and holes injected from each subcell must be aligned to induce facile

recombination. Finally, the ICLs must prevent damage to the underlying layer(s) during processing.

The types of the ICL can be classified into two types, that is, formation using thermal evaporation in vacuum and formation using the solution process. The former is mainly applied to STSCs, and can easily form a multiple layer structure, and the thickness of each layer can be precisely controlled. The typical ICLs processed *via* this method include Au, Ag, Al, MoO_3/Ag/Al/Ca [20], and MoO_x/SnO_x [21]. However, it has a limitation that it takes much time and cost for the process. In the latter case, it is applied to PTSCs mainly using the solution process [22], and it is advantageous in mass-production using roll-to-roll, inkjet, and spray coating. However, such a solution process has a problem in that the underlying organic layer(s) may be damaged during the formation of the ICL.

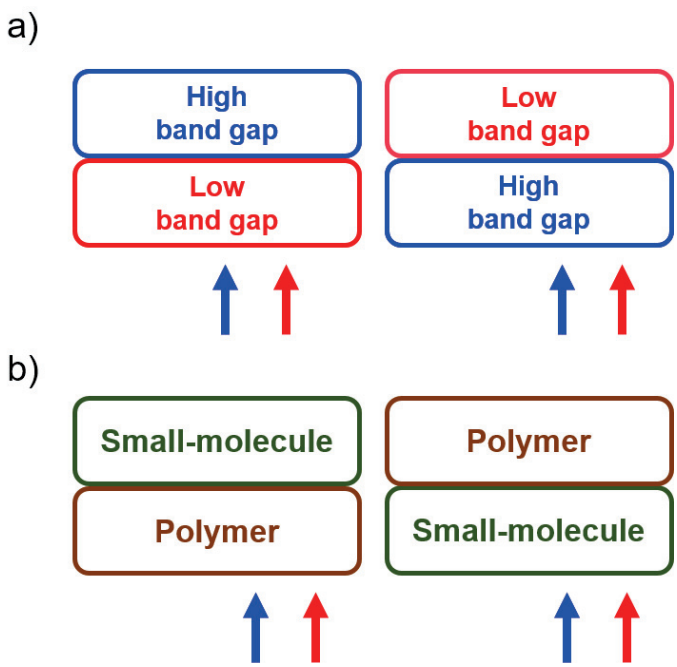

Figure 1.6 Various arrangement of light-absorbing materials for efficient photon absorption (a) high-bandgap – low-bandgap material combinations. (b) small-molecule- – polymer-based material combinations.

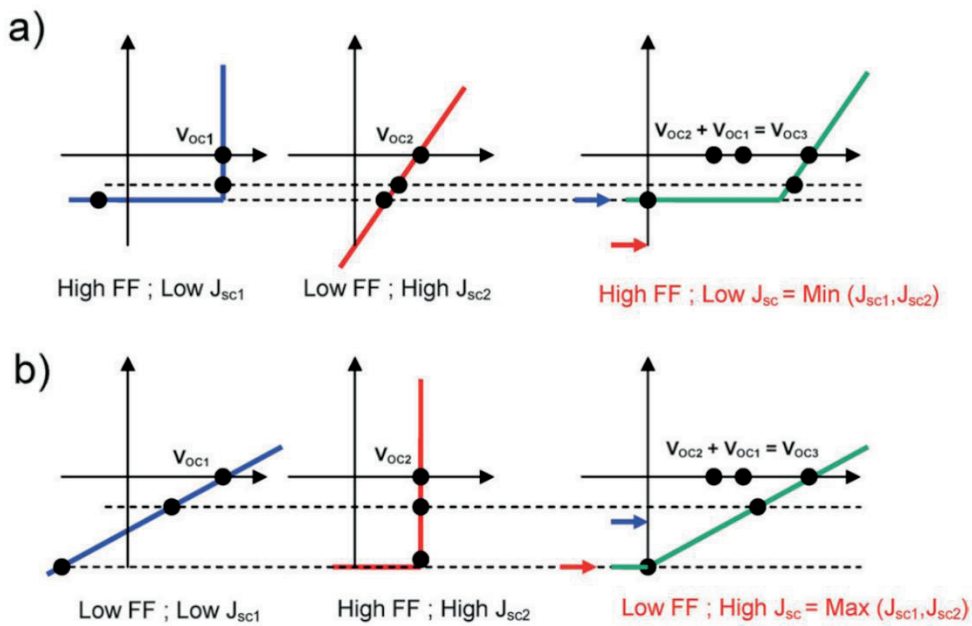

Figure 1.7 (a) The combination of a device with lower J_{SC} and significantly higher FF and a device with higher J_{SC} and extremely low FF results in a tandem cell with a J_{SC} = Min(J_{SC1}, J_{SC2}). (b) The combination of a device with extremely low FF and lower J_{SC} and a device with very good FF and higher J_{SC} leads to a tandem device with a J_{SC} = Max(J_{SC1}, J_{SC2}). Reprinted with permission from The Royal Society of Chemistry[16].

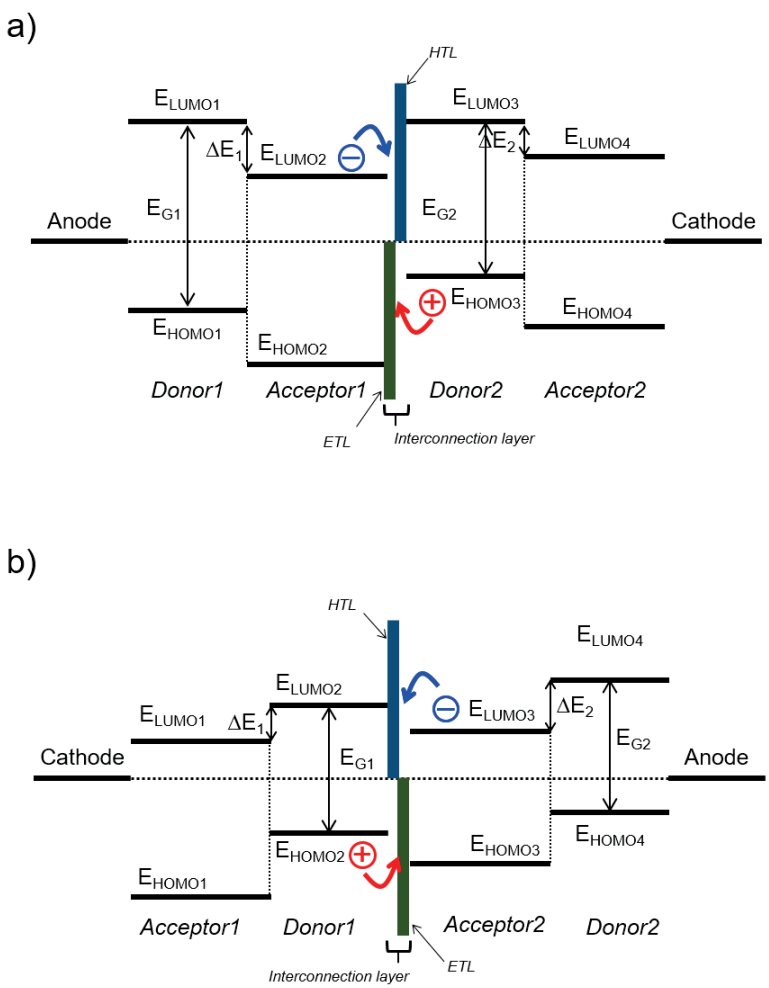

Figure 1.8 Simplified schematic band diagram of tandem solar cells. (a) conventional structure. (b) inverted structure.

1.4 Scope of this thesis

This thesis mainly focuses on the development of the novel thin-film deposition techniques to overcome the limitations of organic solar cells for commercialization. To this end, I will explain the results of research on the following three topics. First, the development of ETL deposition method suitable for the low-temperature solution process. Second, the development of a fabrication process to increase the degree of freedom in the arrangement of the light-absorbing layers of a hybrid OTSCs. Last, I describe a study on the development of ICLs for PTSCs.

In Chapter 2, I will introduce the ZnO thin-film deposition method suitable for the low-temperature solution process. I investigate the effects of annealing temperature (T_A) of ZnO thin-film on the performance of inverted polymer solar cells in which ZnO ETLs are deposited by spin coating aqueous solutions of an ammine-hydroxo zinc complex. Inverted polymer solar cells based on poly(3-hexylthiophene):[6,6]-phenyl-C_{60}-butyric acid methyl ester with T_A as low as 80 °C exhibit a PCE of 3.6%, which is equal to those of devices with higher T_A. Characterizations of the ZnO films using X-ray photoelectron spectroscopy (XPS), ultraviolet photoelectron spectroscopy (UPS), grazing incidence wide-angle X-ray scattering (GI-WAXS), and optical transmittance measurements show that the abrupt improvement of a

device's performance from T_A = 60 °C to 80 °C is due to the improvement of energy-level alignment that arises from the increases in the relative amount and the crystallinity of ZnO. This work has been published as "Effects of annealing temperature of aqueous solution-processed ZnO electron-selective layers on inverted polymer solar cells" by Y. Ka, E. Lee, S. Y. Park. J. Seo, D.-G. Kwon, H. H. Lee, Y. Park, Y. S. Kim, and C. Kim, *Organic electronics,* 14, 100–104 (2013) [23].

In Chapter 3, I demonstrate the improvement of the placement freedom of the light absorption layer of the hybrid OTSC through a thin-film transfer process. Multilayer structures involving solution-deposited polymer films are challenging to fabricate, not allowing for unrestricted designs of polymer-based optoelectronic devices required for maximizing their performance. In this work, I fabricate a hybrid OTSC whose top and bottom subcells have polymer:fullerene and small molecules active layers, respectively, by a solvent-free process based on transferring the polymer:fullerene layer from an elastomeric stamp onto a vacuum-deposited bottom subcell. The interface between small molecule and transferred polymer:fullerene layers is void-free at the nanoscale, allowing for efficient charge transport across the interface. Consequently, the transfer-fabricated tandem cell has a V_{OC} almost identical to the sum of V_{OC} values for the single-junction devices. The J_{SC} of the tandem

cell is maximized by current matching achieved by varying the thickness of the small molecule active layer in the bottom subcell, which is verified by numerical simulations. The results have been published as “Hybrid organic tandem solar cell comprising small molecule bottom and polymer:fullerene top subcells fabricated by thin-film transfer” by Y. Ka, H. Hwang, and C. Kim, *Scientific Reposts*, 7, 1942, (2017) [24].

In Chapter 4, the study on the other application of a thin-film transfer process is explained. The ICLs for PTSCs reported so far are limited in materials’ choice and layer structure, because of a requirement that the ICLs must prevent the penetration of solvents used for the top cells. In this research, it is demonstrated that depositing the active layer of the top subcell using a dry thin-film transfer technique allows for the incorporation of an ICL composed of vacuum-deposited materials in a polymer tandem cell, providing a large degree of freedom in ICL design. This work has been published as “Eliminating the solvent blocking requirement of interconnection layers in polymer tandem solar cells by thin-film transfer technique” by Y. Ka, H. Kim, S. Han, and C. Kim, *Nanoscale* 10, 12588 (2018) [25].

Finally, in chapter 5, the overall conclusion and the potential of this thesis are summarized.

1.5 References

[1] S. Li, L. Ye, W. Zhao, H. Yan, B. Yang, D. Liu, W. Li, H. Ade, J. Hou, A wide band gap polymer with a deep highest occupied molecular orbital level enables 14.2% efficiency in polymer solar cells, J. Am. Chem. Soc., 140 (2018) 7159–7167.

[2] J. Hou, O. Inganas, R. H. Friend, F. Gao, Organic solar cells based on non-fullerene acceptors, Nat. Mater., 17 (2018) 119–128.

[3] G. Zhang, G. Yang, H. Yan, J. H. Kim, H. Ade, W. Wu, X. Xu, Y. Duan, Q. Peng, Efficient nonfullerene polymer solar cells enabled by a novel wide bandgap small molecular acceptor, Adv. Mater., 29 (2017) 1606054-1–1606054-7.

[4] S. Shockley, H. J. Queisser, Detailed balance limit of efficiency of p-n junction solar cells, J. Appl. Phys., 32 (1961) 510–519.

[5] H. Wang, J. Huang, S. Xing, J. Yu, Improved mobility and lifetime of carrier for highly efficient ternary polymer solar cells based on TIPS-pentacene in PTB7: PC71BM, Org. Electron., 28 (2016) 11–19.

[6] S. B. Rim, R. F. Fink, J. C. Schoneboom, P. Erk, P. Peumans, Effect of molecular packing on the exciton diffusion length in organic solar cells, Appl. Phys. Lett., 91 (2007) 173504-1–173504-3.

[7] Z. Tang, Z. George, Z. Ma, J. Bergqvist, K. Tvingstedt, K. Vandewal, E.

Wang, L. M. Andersson, M. R. Andersson, F. Zhang, O. Inganäs, Semi-transparent tandem organic solar cells with 90% internal quantum efficiency, Adv. Energy Mater., 2 (2012) 1467–1476.

[8] Pierre, A. C., Introduction to Sol-Gel Processing, springer, 1 1998.

[9] M. Hiramoto, M. Suezaki, M. Yokoyama, Effect of thin gold interstitial-layer on the photovoltaic properties of tandem organic solar cell, Chem. Lett., 19 (1990) 327–330.

[10] A. Yakimov, S. R. Forrest, High photovoltage multiple-heterojunction organic solar cells incorporating interfacial metallic nanoclusters, Appl. Phys. Lett., 80, (2002) 1667–1669.

[11] Heliatek, http://www.heliatek.com/en/press/press-releases/details/heliatek-consolidates-its-technology-leadership-by-establishing- a-new-world-record-for-organic-solar-technology-with-a-cell-effi (2013).

[12] K. Kawano, N. Ito, T. Nishimori, J. Sakai, Open circuit voltage of stacked bulk heterojunction organic solar cells, Appl. Phys. Lett., 88 (2006) 073514-1–073514-3

[13] J. Gilot, M. M. Wienk, R. A. J. Janssen, Double and triple junction polymer solar cells processed from solution, Appl. Phys. Lett., 90 (2007) 143512-1–143512-3.

[14] J. Y. Kim, K. Lee, N. E. Coates, D. Moses, T.-Q. Nguyen, M. Dante, A.

J. Heeger, Efficient tandem polymer solar cells fabricated by all-solution processing, Science, 317 (2007) 222–225.

[15] L. Meng, Y. Zhang, X. Wan, C. Li, X. Zhang, Y. Wang, X. Ke, Z. Xiao, L. Ding, R. Xia, H.-L. Yip, Y. Cao, Y. Chen, Organic and solution-processed tandem solar cells with 17.3% efficiency, Science 361 (2018) 1094-1098.

[16] T. Ameri, G. Dennler, C. Lungenschmied, C. J. Brabec, Organic tandem solar cells: A review, Energy Environ. Sci., 2 (2009) 347–363.

[17] C. Yan, Y. Wu, J. Wang, R. Li, P. Cheng, H. Bai, Z. Zhan, W. Ma and X. Zhan, Enhancing performance of non-fullerene organic solar cells *via* side chain engineering of fused-ring electron acceptors, Dyes Pigm., 139 (2017) 627–634.

[18] Y. Lin, F. Zhao, Y. Wu, K. Chen, Y. Xia, G. Li, S. K. Prasad, J. Zhu, L. Huo, H. Bin, Z. G. Zhang, X. Guo, M. Zhang, Y. Sun, F. Gao, Z. Wei, W. Ma, C. Wang, J. Hodgkiss, Z. Bo, O. Inganas, Y. Li, X. Zhan, Mapping polymer donors toward high-efficiency fullerene free organic solar cells, Adv. Mater., 29 (2017) 1604155-1–1604155-9.

[19] Y. Lin, J. Wang, Z. G. Zhang, H. Bai, Y. Li, D. Zhu, X. Zhan, An electron acceptor challenging fullerenes for efficient polymer solar cells, Adv. Mater., 27 (2015) 1170–1174.

[20] D. W. Zhao, L. Ke, Y. Li, S. T. Tan, A. K. K. Kyaw, H. V. Demir, X. W.

Sun, D. L. Carroll, G. Q. Lo, D. L. Kwong, Optimization of inverted tandem organic solar cells, Sol. Energy Mater. Sol. Cells, 95 (2011) 921–926.

[21] T. Becker, S. Trost, A. Behrendt, I. Shutsko, A. Polywka, P. Görrn, P. Reckers, C. Das, T. Mayer, D. Di Carlo Rasi, K. H. Hendriks, M. M. Wienk, R. A. J. Janssen, T. Riedl, All-oxide MoO_x/SnO_x charge recombination interconnects for inverted organic tandem solar cells, Adv. Energy Mater., 8 (2018) 1702533-1–1702533-8.

[22] N. Li, D. Baran, K. Forberich, M. Turbiez, T. Ameri, F. C. Krebs, C. J. Brabec, An Efficient solution-processed intermediate layer for facilitating fabrication of organic multi-junction solar cells, Adv. Energy Mater., 3 (2013) 1597–1605.

[23] Y. Ka, E. Lee, S. Y. Park. J. Seo, D.-G. Kwon, H. H. Lee, Y. Park, Y. S. Kim, C. Kim, Effects of annealing temperature of aqueous solution-processed ZnO electron-selective layers on inverted polymer solar cells, Org. Electron., 14 (2013) 100–104.

[24] Y. Ka, H. Hwang, C. Kim, Hybrid organic tandem solar cell comprising small-molecule bottom and polymer:fullerene top subcells fabricated by thin-film transfer, Sci. Rep., 7 (2017) 1942-1–1942-8.

[25] Y. Ka, H. Kim, S. Han, C. Kim, Eliminating the solvent blocking requirement of interconnection layers in polymer tandem solar cells by thin-

film transfer technique, Nanoscale, 10 (2018) 12588–12594.

Chapter 2 Solution-processed ZnO thin-film deposition for electron transport layer of inverted polymer solar cells

2.1 Overview

ZnO, one of the conventional metal oxide materials, has been widely used as an n-type semiconductor of thin-film transistors or solar cells. This is because ZnO has high transmittance in the visible region and a high electron mobility (~ 2000 $cm^2/(V \cdot s)$ @80K) and can form a large-area thin-film through a solution process [1]. Sol-gel based zinc acetate method [2–4] and ZnO nanoparticle method [5–8] are well-known solution process methods of ZnO which has been widely used. The zinc acetate method has a mechanism to form a ZnO thin-film by spin-coating zinc acetate complex based precursor solution followed by heating. In the case of ZnO nanoparticle method, the nanoparticle dispersion is spin-coated on a substrate to form a thin-film, or a substrate is dipped in the nanoparticle dispersion to form a ZnO thin-film. All of these ZnO deposition methods have an advantage that a large-area thin-film can be formed easily through a solution process.

The ZnO thin-film applied to the electron transport layer (ETL) of the flexible device, or the interconnection layer (ICL) of the organic tandem solar

cell should satisfy the following conditions in the process. First, it should have a process temperature that does not damage plastic substrates with a low glass transition temperature (PET: 60 ~ 80 ºC, PEN: ~120 ºC). Next, when used in ICL of an organic tandem solar cell, organic solvents damaging the underlying organic layer are not used, and a high heat treatment process is not required. From these criteria, the zinc acetate method and the ZnO nanoparticle method described above have various limitations. First, the zinc acetate method has a limitation that it is difficult to apply to a plastic substrate or an organic layer because thermal annealing at a temperature higher than 300 °C is required for forming a ZnO thin-film from a precursor material (Fig. 2.1a). The ZnO nanoparticle method can form ZnO thin-film at a process temperature as low as 150 ºC. However, this method requires ligands to prevent ZnO nanoparticles from aggregating in solution (Fig. 2.1b) [8]. Meyers et al. have demonstrated that ZnO thin-film transistors with mobilities up to 1.8 $cm^2/V{\cdot}s$ can be fabricated by spin-coating an aqueous solution of ammine-hydroxo zinc complex, $Zn(OH)_2(NH_3)_x$, and subsequent annealing at 150 °C [9]. The authors claimed that annealing at 150 °C provides sufficient energy to obtain ZnO from the complex by ammonia dissociation, dehydration, followed by crystallization:

$$Zn(OH)_2(NH_3)_x(aq) \rightarrow ZnO(s) + xNH_3(g) + H_2O(g) \quad (1)$$

Recently, this method has been successfully employed to deposit a ZnO ETL at 150 °C in inverted polymer solar cells (IPSCs) based on poly(3-hexylthiophene) (P3HT):[6,6]-phenyl-C_{60}-butyric acid methyl ester ($PC_{60}BM$) [10,11]. Here, I fabricate IPSCs based on P3HT:$PC_{60}BM$, whose ZnO ETLs are deposited by spin coating an aqueous solution of the ammine-hydroxo zinc complex [9], followed by thermal annealing at a temperature ranging from 25 °C to 150 °C. I demonstrate that devices with the annealing temperature as low as 80 °C exhibit η_p = 3.6%, which is equal to that of devices annealed at higher temperatures, showing that the ZnO deposition method is well-suited for the fabrication of organic solar cells on flexible substrates. The characterization of the ZnO films using X-ray photoelectron spectroscopy (XPS), grazing incidence wide-angle X-ray scattering (GI-WAXS), ultraviolet photoelectron spectroscopy (UPS), and optical transmittance spectrum measurements show that in the temperature range of 60 °C to 90 °C, the relative amount of ZnO and its crystallinity increase, and the energy-level alignment improves, leading to an abrupt improvement in solar cell performance.

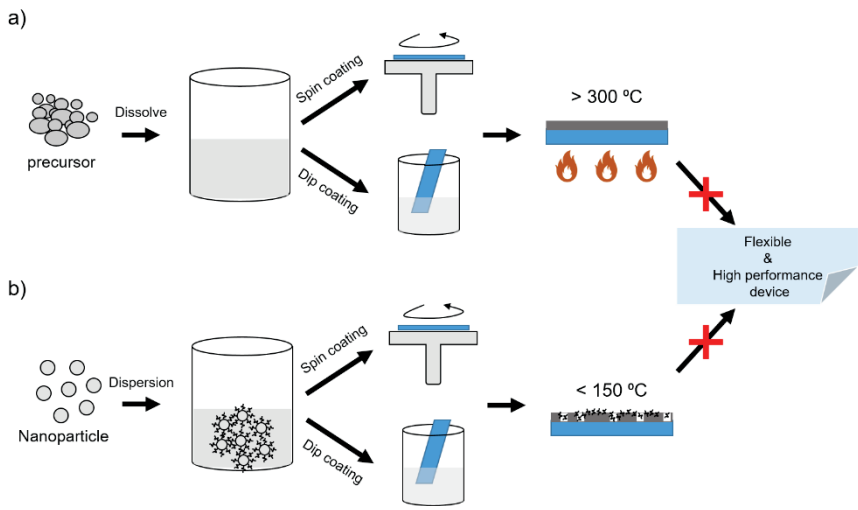

Figure 2.1 Common ZnO thin-film deposition methods. a) Sol−gel based ZnO thin-film deposition method. b) ZnO nanoparticle method.

2.2 Effects of ZnO annealing temperatures on device performance

Figure 2.2 (inset) shows the structure of an IPSC with a ZnO ETL, which was deposited by spin coating an aqueous solution of the ammine-hydroxo zinc complex [9] on a precleaned glass substrate coated with ITO. The aqueous precursor solutions of the ammine-hydroxo zinc complex were prepared following procedures described elsewhere [9]. Prior to the spin coating of the precursor solution at 3000 rpm for 30 s, the ITO surface was treated with UV-ozone. Then, the sample (glass/ITO/ZnO) was annealed in an N_2-filled glove box at different temperatures – 25 (not annealed), 60, 70, 80, 90, and 150 °C for 30 min. The thicknesses of the ZnO films were approximately 8 nm. The active layer composed of P3HT:$PC_{60}BM$ was deposited by spin coating its solution in 1,2-dichlorobenzene. The bulk-heterojunction morphology was improved by ‘‘solvent annealing’’ for 120 min, and the resulting thickness was ~ 220 nm. Next, 12-nm-thick molybdenum oxide (MoO_3) and 100-nm-thick Ag layers were deposited as hole transport and anode layers, respectively, by thermal evaporation in high vacuum ($< 7 \times 10^{-7}$ Torr). Current density versus voltage (*J–V*) characteristics were measured using a Keithly 2400 source meter and a solar simulator (L01, Peccell) calibrated with a standard silicon solar cell (BS-520, Bunkoukeiki Co., Ltd.).

Figure 2.2 shows the current density versus voltage (*J–V)* characteristics, under simulated 1sun AM1.5G illumination, of IPSCs with different ZnO annealing temperatures (T_A), whose performances are summarized in Table 1. The *J–V* curves of the devices with T_A =25 °C and 60 °C exhibit the S-shape feature [12], indicating that photo-generated excitons are converted into charge carriers collected at the electrodes with a very low probability, which increases with negative bias. As a result, power-conversion efficiency (PCE) of these devices is less than 0.2%. An increase in T_A to 70 °C resulted into an abrupt change in *J–V* characteristics, leading to short-circuit current density (J_{SC}) = 9.7 mA cm^{-2}, open-circuit voltage (V_{OC}) = 0.59 V, fill factor (FF) = 0.49, and PCE = 2.6%. A further increase in T_A (= 80 °C) increased PCE to 3.6%, which is mainly attributed to increased FF (= 0.61). Almost identical results were obtained for devices with T_A > 80 °C. For example, devices with T_A = 150 °C have J_{SC} = 10.0 mA cm^{-2}, V_{OC} = 0.59 V, FF = 0.62, and PCE = 3.6%. The *J–V* characteristics in the dark (Fig. 2.3) show a similar trend: devices with $T_A \geq 80$ °C have almost identical characteristics, whose current densities are much larger than those of devices with $T_A \leq 60$ °C, while devices with T_A = 70 °C show a transition between these two sets.

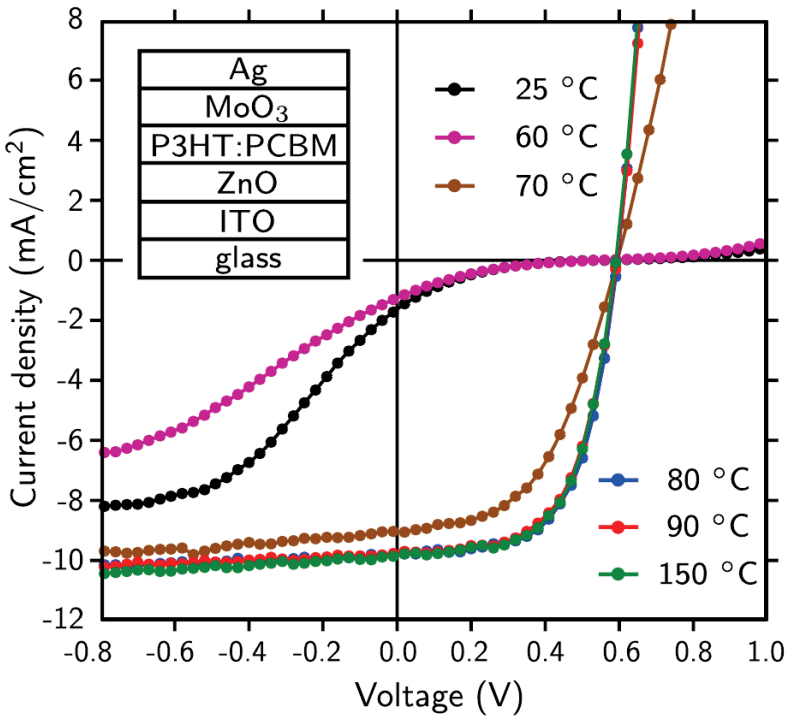

Figure 2.2 Current density–voltage characteristics of inverted polymer solar cells (IPSCs) with a ZnO electron transport layer (ETL) under simulated 1 sun AM1.5G illumination. The ZnO ETLs were deposited by spin coating an aqueous solution of an ammine-hydroxo zinc complex, followed by thermal annealing at different temperatures. Inset: Structure of the IPSCs.

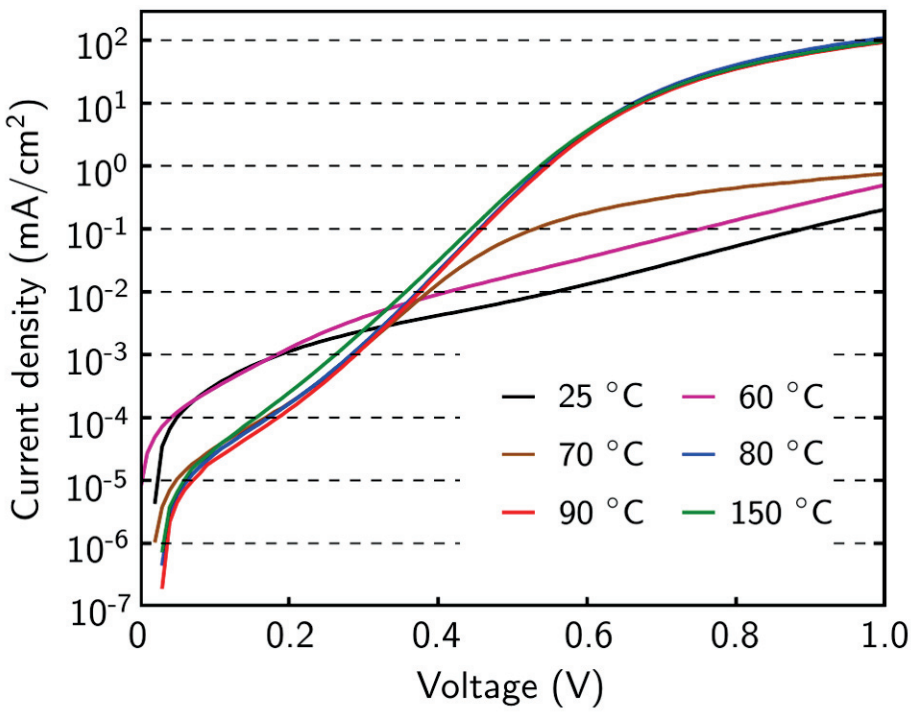

Figure 2.3 Current density – voltage characteristics of inverted polymer solar cells with a ZnO electron transport layer in the dark.

Table 1 Comparison of performance of inverted polymer solar cells with ZnO electron transport layers annealed at different temperatures. The device parameters are values averaged over more than ten devices for each annealing temperature.

Temp. (°C)	J_{SC} (mA cm^{-2})	V_{OC} (V)	**FF**	**PCE** (%)
25	1.7±0.7	0.53±0.02	0.14±0.02	0.14±0.03
60	2.0±0.7	0.52±0.02	0.13±0.01	0.10±0.04
70	9.7±0.8	0.59±0.01	0.49±0.06	2.6±0.4
80	9.8±0.1	0.59	0.61±0.02	3.6±0.1
90	9.8±0.1	0.59	0.62±0.01	3.6±0.1
150	10.0±0.3	0.59±0.01	0.62±0.01	3.6±0.1

2.3 Characterizations of ZnO thin-films: the origins of T_A dependency of device performance

To identify the origins of the effects of T_A on the device performance, I first performed XPS measurements on ZnO films deposited on ITO-coated glass substrates using the same procedure used in the IPSC fabrication. Figure 2.4 shows the O 1s core level spectra of the samples with different T_A (= 25, 60, 90, and 150 °C), where the measured data (solid symbols) were fitted by two Gaussian functions centered at 530.9 ± 0.1 eV and 532.5 ± 0.4 eV. The signals around the lower-energy peak are attributed to oxygen atoms in the ZnO wurtzite structure and those in oxygen-deficient regions within the ZnO matrix, whose peak binding energies are reported to be 530.15 eV and 531.25 eV, respectively [13]. A higher binding energy (= 533 eV), which is similar to the higher-energy peak in Fig. 2.4, has been reported to be also associated with oxygen deficiency [4,14]. Considering Eq. (1) and that the higher energy peak is more pronounced for samples with lower T_A, I conclude that it is attributed to oxygen atoms in $Zn(OH)_2$ [15] and/or $Zn(OH)_2(NH_3)_x$, which were present due to the lack of thermal energy required for the reaction in Eq. (1) to occur completely. The increase in the relative amount of ZnO with T_A, shown in Fig. 2.4, is consistent with previous X-ray diffraction [16] and XPS [17] analyses performed on ZnO films deposited by chemical bath deposition based on the

same chemistry. Photoelectron spectroscopy measurements were performed using a modified KRATO AXIS-165 system, where He I (21.2 eV) and Mg K_α (1253.6 eV) sources were employed for XPS experiments, respectively [26]. The base pressure of the analysis chamber was 1×10^{-9} Torr.

Figure 2.5 shows the GI-WAXS patterns of the ZnO films on ITO-coated glass substrates annealed at 25, 60, 90, and 150 °C. GI-WAXS patterns were obtained using synchrotron X-ray with a wavelength (λ) of 1.3590 Å from the beam line 5A in Pohang Accelerator Laboratory, Korea. Since the film thicknesses were very small (< 10 nm), no peaks other than those attributed to ITO were detected using conventional theta–2theta scans with Cu Kα radiation (λ = 1.5406 Å). The GI-WAXS peaks corresponding to (100), (002), and (101) orientations of the ZnO wurtzite structure, which are marked by arrows, appeared only for the samples with T_A =90 °C and 150 °C. For all samples, GI-WAXS peaks arising from $Zn(OH)_2$ were absent [16,18]. The values of d-spacing corresponding to the (100), (002), and (101) peaks are, respectively, 0.9%, 0.7%, and 0.3% smaller than those for a bulk wurtzite crystal, which are possibly due to the small size of the nanocrystals and/or residual stress in the film.

Figure 2.6 shows the transmittance spectra of the ZnO films deposited on fused silica substrates by the aqueous solution method. Optical transmittance

data were obtained using a UV–vis–NIR spectrophotometer (Cary 5000, Varian Inc.). As T_A increases, the transmission dip occurring at $\lambda \geq 210$ nm for T_A 70 °C disappears, with another dip at $\lambda \approx 335$ nm observed for the samples with $T_A \geq 70$ °C becoming increasingly pronounced. The transmission dip at $\lambda \approx 335$ nm is due to excitonic transitions in ZnO nanocrystals [19], consistent with data reported for ZnO films deposited by other solution-based methods [3,20]. Considering the chemical reaction in Eq. (1), the transmission dip at $\lambda \approx 210$ nm is possibly attributed to $Zn(OH)_2$, $Zn(OH)_2(NH_3)_x$, or amorphous ZnO, which may be present in the films due to incomplete dehydration, ammonia dissociation, or ZnO crystallization. Since the absorption edge of amorphous ZnO thin-films were reported to be $\lambda >> 210$ nm [21, 22], and the transmittance spectrum of $Zn(OH)_2$ precipitates obtained in preparing the aqueous solution of $Zn(OH)_2(NH_3)_x$ [9] does not show such a dip, the absorption near $\lambda \sim 210$ nm is likely due to $Zn(OH)_2(NH_3)_x$. The values of the optical band gap (E_{opt})of the ZnO layers estimated from the transmittance spectra are 5.60 (25 °C), 5.52 (60 °C), 3.47 (70 °C), 3.45 (80 °C), 3.47 (90 °C), and 3.46 eV (150 °C), as shown in Fig. 2.6. In the spectral region of $\lambda \geq 400$ nm, the values of transmittance are larger than 90% (96% when normalized with respect to the transmittance of the fused silica substrate) for the samples with all T_A shown in Fig. 2.7. In Fig. 2.8, I show the UPS spectra for the ZnO

films on ITO-coated glass substrates annealed at different temperatures. The work functions determined from the secondary electron cutoffs (left panel, Fig. 2.8) are 3.69, 3.72, 4.08, and 4.09 eV for T_A of 25, 60, 90 and 150 °C, respectively, confirming the abrupt transitions between 60 °C and 90 °C observed in the GI-WAXS and transmittance data. The same is true for the valence band maximum (VBM) determined from the photoemission onset on the right panel of Fig. 2.8 (measured using same environment as XPS data measurement): the values of VBM are 3.95, 3.88, 3.55, and 3.51 eV below the Fermi level (E_F), for T_A of 25, 60, 90, and 150 °C, respectively. From the values of E_{opt} extracted from the transmittance data, the conduction band minimum (CBM) of the ZnO films with $T_A \geq 70$ °C is estimated to be located near E_F and the LUMO of $PC_{60}BM$. This energy-level alignment facilitates electron injection into, and extraction from $PC_{60}BM$, consistent with a large forward current and a large photocurrent. The relatively poor performance of the IPSCs with T_A =70 °C may be due to smaller amount and/or size of ZnO nano-crystals, which may decrease the number of percolation pathways for electron transport through ZnO. The large values of E_{opt} (> 5.5 eV) for the ‘‘ZnO’’ films with $T_A \leq 60$ °C mean that charge-transport levels in these films are located much higher (close to the vacuum level) than CBM of ZnO films with $T_A \geq 70$ °C, assuming that they are located near VBM + E_{opt}. This

indicates that the IPSCs with $T_A \leq 60$ °C have a large energy barrier for electron injection from the ITO to the ZnO, consistent with very small currents in the forward bias region (> ~ 0.6 V). In addition, they also have a large energy barrier for extracting photo-generated electrons from the LUMO of $PC_{60}BM$ to the ZnO, leading to a small photocurrent that increases with reverse bias. The conductivity values of the ZnO films, obtained from the current–voltage characteristics measured in a two-point configuration [23], were 8.6×10^{-7}, 1.0×10^{-6}, 1.0×10^{-6}, 1.1×10^{-6} S/cm for $T_A = 25$, 60, 90, and 150 °C, respectively. Considering small ZnO thicknesses (<10 nm), the differences in conductivity values are too small to explain the marked contrast in the *J–V* characteristics between devices with $T_A \leq 60$ °C and $T_A \geq 80$ °C.

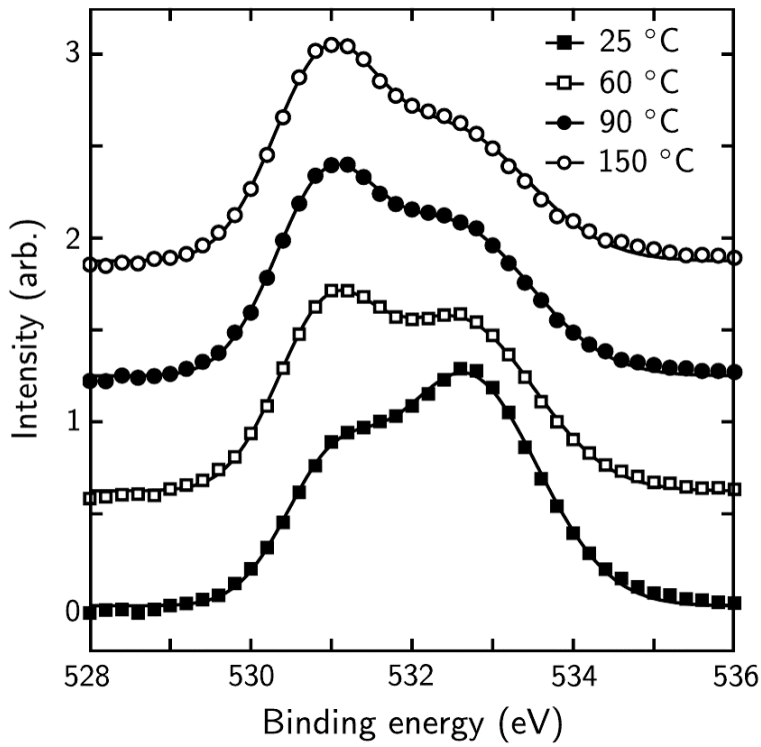

Figure 2.4 O 1s XPS spectra of ZnO films on ITO-coated glass substrates, annealed at 25 °C (filled squares), 60 °C (open squares), 90 °C (filled circles), and 150 °C (open circles). Solid lines are fits to the experimental data by two Gaussian functions centered at 530.9 ± 0.1 eV and 532.5 ± 0.4 eV.

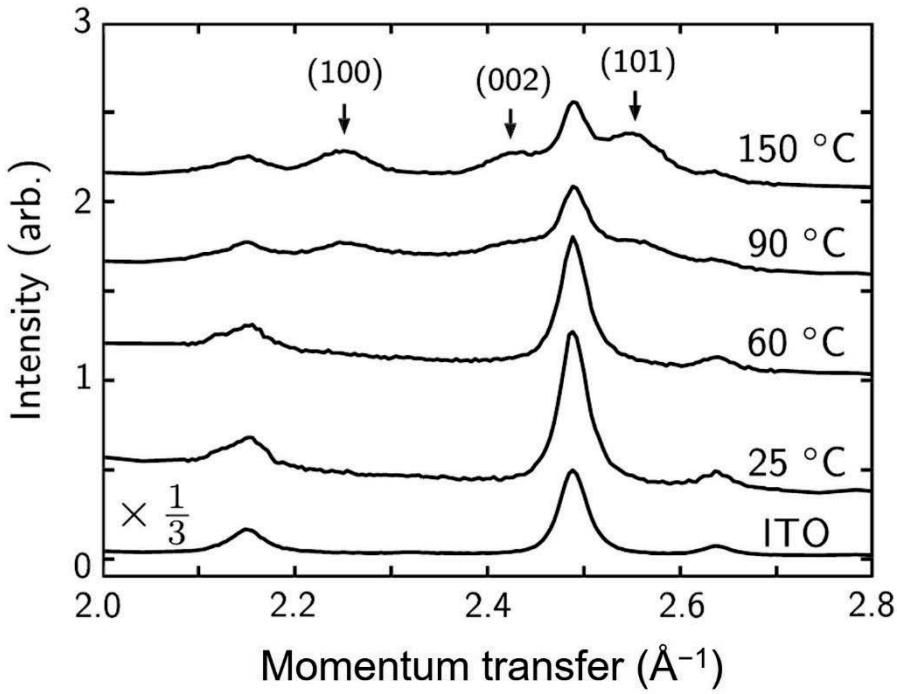

Figure 2.5 Grazing incidence wide-angle X-ray scattering patterns of the ZnO films on ITO-coated glass substrates. The patterns were vertically displaced for clarity, and the pattern for an ITO-coated glass substrate without a ZnO film was reduced by a factor of three.

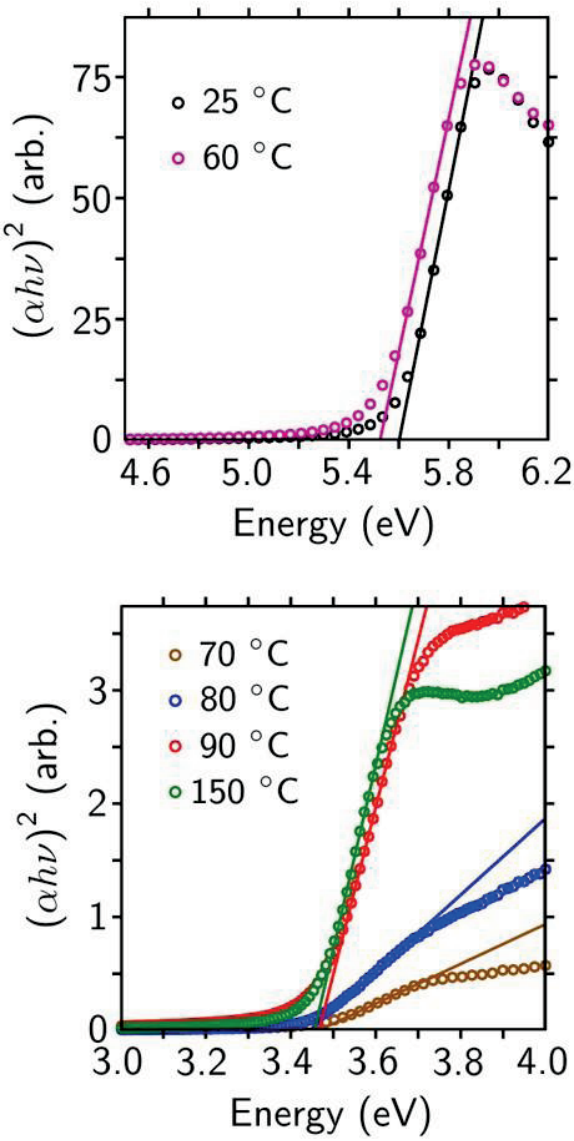

Figure 2.6 $(\alpha hv)^2$ versus photon energy, where α is the absorption coefficient extracted from the transmittance spectra shown in Fig. 2.6, h is planck's constant, and v is the frequency of photons. Solid lines are linear fits to $(\alpha hv)^2$.

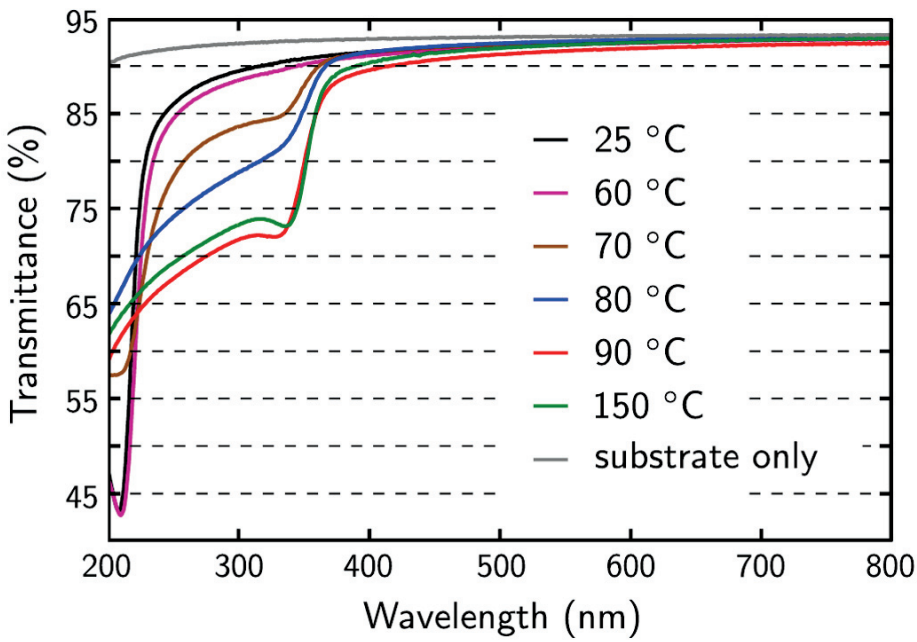

Figure 2.7 Transmittance spectra of ZnO films spin coated on fused silica substrates, annealed at different temperatures. Also shown is the transmittance spectrum of a fused silica substrate.

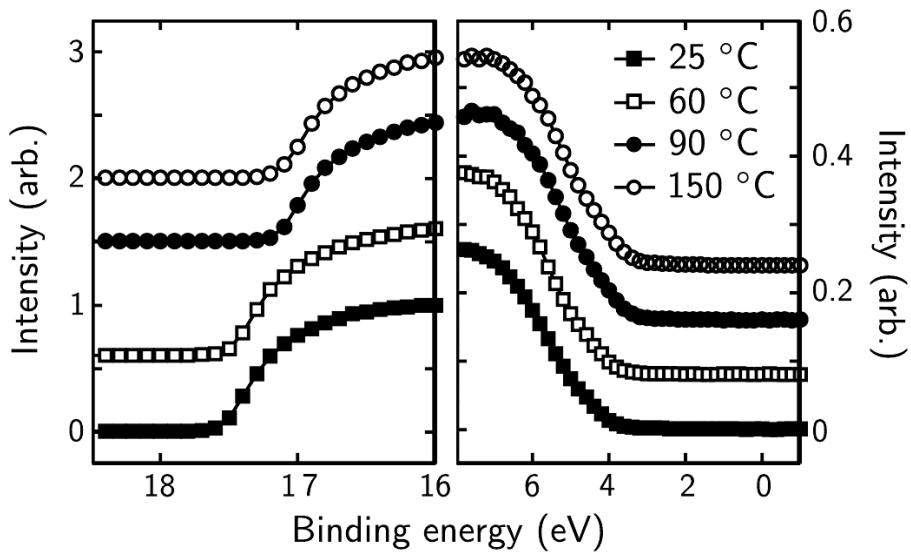

Figure 2.8 UPS spectra of ZnO films on ITO-coated glass substrates, annealed at 25 °C (filled squares), 60 °C (open squares), 90 °C (filled circles), and 150 °C (open circles).

2.4 Conclusion

In summary, I fabricated inverted polymer solar cells based on P3HT:$PC_{60}BM$ with ZnO electron transport layers deposited by spin coating an aqueous solution of ammine-hydroxo zinc complex, $Zn(OH)_2(NH_3)_x$, and investigated the effects of the ZnO annealing temperature (T_A) on device performance. While devices with $T_A \leq 60$ °C had power conversion efficiencies (PCE) smaller than 0.20%, normal solar cell operation was achieved with T_A as low as 80 °C, yielding PCE = 3.6%. The characterization of the ZnO films showed that the abrupt improvement in solar cell performance from $T_A = 60$ to 80 °C is attributed to the improvement in the energy-level alignment arising from the increases in the relative amount and the crystallinity of ZnO. The ZnO deposition method based on the aqueous solution of the ammine-hydroxo zinc complex is well-suited for the fabrication of organic solar cells on flexible substrates.

2.5 References

[1] H.-L. Yip, A. K.-Y. Jen, Recent advances in solution-processed interfacial materials for efficient and stable polymer solar cells, Energy Environ. Sci., 5 (2012) 5994–6011.

[2] M. S. White, D. C. Olson, S. E. Shaheen, N. Kopidakis, D. S. Ginley, Inverted bulk-heterojunction organic photovoltaic device using a solution-derived ZnO underlayer, Appl. Phys. Lett., 89 (2006) 143517.

[3] A. K. K. Kyaw, X. W. Sun, C. Y. Jiang, G. Q. Lo, D. W. Zhao, D. L. Kwong, An inverted organic solar cell employing a sol–gel derived ZnO electron selective layer and thermal evaporated MoO_3 hole selective layer, Appl. Phys. Lett., 93 (2008) 221107.

[4] Y. Sun, J.H. Seo, C.J. Takacs, J. Seifter, A.J. Heeger, Inverted polymer solar cells integrated with a low-temperature-annealed sol–gel- derived ZnO film as an electron transport layer, Adv. Mater, 23 (2011) 1679–1683.

[5] S. K. Hau, H.-L. Yip, N. S. Baek, J. Zou, K. O'Malley, A. K.-Y. Jen, Air-stable inverted flexible polymer solar cells using zinc oxide nanoparticles as an electron selective layer, Appl. Phys. Lett., 92 (2008) 253301.

[6] C. Pacholski, A. Kornowski, H. Weller, Self-assembly of ZnO: from nanodots to nanorods, Angew Chem. Int. Edit., 41 (2002) 1188–1191.

[7] W. Beek, M.M. Wienk, M. Kemerink, X.N. Yang, R. Janssen, Hybrid zinc

oxide conjugated polymer bulk heterojunction solar cells, J. Phys. Chem. B, 109 (2005) 9505–9516.

[8] F.C. Krebs, Y. Thomann, R. Thomann, J.W. Andreasen, A simple nanostructured polymer/ZnO hybrid solar cell – preparation and operation in air, Nanotechnology, 19 (2008) 424013.

[9] S. Meyers, J. Anderson, C. Hung, J. Thompson, J. Wager, D. Keszler, Aqueous inorganic inks for low-temperature fabrication of ZnO TFTs, J. Am. Chem. Soc., 130 (2008) 17603–17609.

[10] S. Bai, Z. Wu, X. Xu, Y. Jin, B. Sun, X. Guo, S. He, X. Wang, Z. Ye, H. Wei, X. Han, W. Ma, Inverted organic solar cells based on aqueous processed ZnO interlayers at low temperature, Appl. Phys. Lett., 100 (2012) 203906-1–203906-4.

[11] Y. Ka, E. Lee, S.Y. Park, Y.S. Kim, C. Kim, Low-temperature fabrication of ZnO-based inverted organic solar cells, SPIE Photonics Europe, 2012, Brussels, Belgium.

[12] W. Tress, K. Leo, M. Riede, Influence of hole-transport layers and donor materials on open-circuit voltage and shape of I–V curves of organic solar cells, Adv. Funct. Mater., 21 (2011) 2140–2149.

[13] M. Chen, X. Wang, Y.H. Yu, Z.L. Pei, X.D. Bai, C. Sun, R.F. Huang, L.S. Wen, X-ray photoelectron spectroscopy and auger electron spectroscopy

studies of Al-doped ZnO films, Appl. Surf. Sci., 158 (2000) 134–140.

[14] X. Q. Wei, B. Y. Man, M. Liu, C. S. Xue, H. Z. Zhuang, C. Yang, Blue luminescent centers and microstructural evaluation by XPS and Raman in ZnO thin films annealed in vacuum, N_2 and O_2, Physica B: Condensed Matter, 388 (2007) 145–152.

[15] S. Kobayashi, K. Oshima, T. Sasaki, N. Tsuboi, F. Kaneko, Effects of annealing on chemical composition, crystallinity, optical transmission and electrical conductivity of ZnO thin films prepared on glass substrates by chemical bath deposition, Jpn. J. Appl. Phys., 44 (2005) 1372–1375.

[16] S. M. Pawar, K. V. Gurav, S. W. Shin, D. S. Choi, I. K. Kim, C. D. Lokhande, J. I. Rhee, J. H. Kim, Effect of bath temperature on the properties of nanocrystalline ZnO thin films, J. Nanosci. Nanotechnol., 10 (2010) 3412–3415.

[17] T. Nii, I. Sugiyama, T. Kase, M. Sato, Y. Kaniyama, S. Kuriyagawa, K. Kushiya, H. Takeshita, Effects of Cd-free buffer layer for $CuInSe_2$ thin-film solar cells, IEEE First world conference on photovoltaic energy conversion, (1994) 254–257.

[18] R. A. McBride, J. M. Kelly, D. E. McCormack, Growth of well-defined ZnO microparticles by hydroxide ion hydrolysis of zinc salts, J. Mater. Chem., 13 (2003) 1196–1201.

[19] R. Viswanatha, S. Sapra, B. Satpati, P.V. Satyam, B.N. Dev, D.D. Sarma, Understanding the quantum size effects in ZnO nanocrystals, J. Mater. Chem., 14 (2004) 661–668.

[20] H. Oh, J. Krantz, I. Litzov, T. Stubhan, L. Pinna, C.J. Brabec, Comparison of various sol–gel derived metal oxide layers for inverted organic solar cells, Sol. Energy Mater. Sol. Cells, 95 (2011) 2194–2199.

[21] J. M. Khoshman, M. E. Kordesch, Optical constants and band edge of amorphous zinc oxide thin films, Thin Solid Films, 515 (2007) 7393– 7399.

[22] A. Dejneka, I. Aulika, M. V. Makarova, Z. Hubicka, A. Churpita, D. Chvostova, L. Jastrabik, V. A. Trepakov, Optical spectra and direct optical transitions in amorphous and crystalline ZnO thin films and powders, J. Electrochem. Soc., 157 (2010) G67–G70.

[23] S. Lim, D. Han, H. Kim, S. Lee, S. Yoo, Cu-based multilayer transparent electrodes a low-cost alternative to ITO electrodes in organic solar cells, Sol. Energy Mater. Sol. Cells, 101 (2012) 170–175.

[24] E. Lee, J. Kim, C. Kim, Polymer tandem photovoltaic cells with molecularly intimate interfaces achieved by a thin-film transfer technique, Sol. Energy Mater. Sol. Cells, 105 (2012) 1–5.

[25] G. Li, Y. Yao, H. Yang, V. Shrotriya, G. Yang, Y. Yang, ‘‘Solvent annealing’’ effect in polymer solar cells based on poly(3- hexylthiophene) and

methanofullerenes, Adv. Funct. Mater., 17 (2007) 1636–1644.

[26] Y.-K. Kim, J.W. Kim, Y. Park, Energy level alignment at a charge generation interface between 4,4'-bis(N-phenyl-1- naphthylamino)biphenyl and 1,4,5,8,9,11-hexaazatriphenylene– hexacarbonitrile, Appl. Phys. Lett., 94 (2009) 063305-1–063305-3.

Chapter 3 Arrangement of the absorption layer in hybrid tandem solar cells using dry thin-film transfer printing

3.1 Overview

Organic solar cells (OSCs) have potentials for lightweight, low-cost, and renewable energy sources [1−4], but they have relatively low power conversion efficiencies (PCEs) compared with those made of inorganic semiconductors such as silicon- or CIGS-based solar cells [5]. In order to increase the PCE of OSCs, many studies focusing on materials [6−8], device structures [9,10], and fabrication techniques [11,12] have been reported. A particularly effective strategy is to use a tandem structure, where multiple single cells absorbing complementary spectral ranges are stacked [13−16]. Depending on the materials used, organic tandem solar cells fall into three categories: polymer [13,17−19], small molecule [20, 21], and hybrid [22] solar cells using both polymer and small molecule materials. The attractive feature of hybrid organic tandem solar cells is that active materials can be chosen from a large number of candidates encompassing various polymers and small molecules. Therefore, using both polymer and small molecule materials, it is

easier to realize organic tandem cells with constituent subcells having complementary absorption spectra, which minimizes the thermalization loss if a device design is such that higher (and lower) energy photons are absorbed in the subcell with a higher (and lower) open-circuit voltage (V_{OC}). Despite this advantage, the highest power conversion efficiency (PCE) of hybrid tandem solar cells reported so far is 4.8% [22], while tandem devices based on polymers and small molecules, respectively, have achieved PCEs as high as 10.6% [15] and 12% [23]. The relatively slow development in hybrid organic tandem solar cells is in part due to the following restriction on the device architecture. Since small molecule materials can easily be degraded or dissolved by solvents used in spin-coating of polymers [24], polymer layers must be deposited on substrates prior to the deposition of small molecules, which is typically achieved by thermal evaporation in vacuum (Fig. 3.1). This is a constraint on the hybrid tandem solar cell having a configuration that allows the light absorbing layer material having a complementary absorption spectrum to efficiently absorb the photons. [25].

Here, I demonstrate a hybrid organic tandem solar cell comprising a polymer:fullerene-based top subcell and a small molecule-based bottom subcell using a thin-film transfer [12,26–28], where an active layer of the top subcell is transferred from an elastomeric stamp onto the bottom subcell. The

bottom subcell with an light-absorbing layer composed of (5,6)-Fullerene-C_{70} (C_{70}) mixed with Di-[4-(N,N-di-p-tolyl-amino)-phenyl]cyclohexane (TAPC) mainly absorbs in the short wavelength region, while the top subcell, whose light-absorbing layer is composed of poly[2,1,3-benzothiadiazole-4,7-diyl[4,4-bis(2-ethylhexyl)-4H-cyclopenta[2,1-b:3,4-b′]dithiophene-2,6-diyl]] (PCPDTBT) mixed with [6,6]-Phenyl-C_{70}-butyric acid methyl ester ($PC_{70}BM$), absorbs in the relatively longer wavelength region that cannot be absorbed in the bottom subcell (Fig. 3.2). The value of V_{OC} for the tandem cell fabricated by the thin-film transfer technique is 1.46 V, which is almost identical to the sum of V_{OC}'s of single-junction devices. The PCE of the tandem cell is 6.26%, which is, to the best of my knowledge, the highest among small molecule–polymer hybrid tandem solar cells demonstrated so far [22]. These results are attributed to the fact that the interface between the PCPDTBT:$PC_{70}BM$ and a small molecule layer formed by thin-film transfer is defect-free at the nanoscale, as was confirmed by cross-sectional transmission electron microscopy (TEM). My work shows that the thin-film transfer technique is capable of overcoming the restriction present in designing small molecule–polymer tandem solar cells, that is, the polymer subcell must be at the bottom, thereby allowing for the maximal utilization of materials space that small molecules and polymers offer in combination.

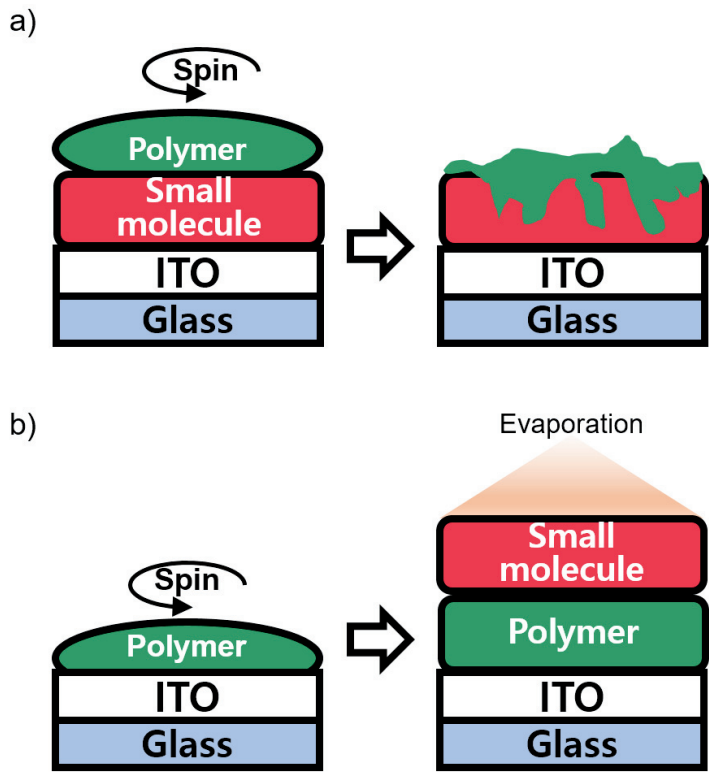

Figure 3.1 Possibility of implementation of device according to arrangement of light absorbing materials of hybrid tandem solar cell. (a) Tandem device of small-molecular–polymer arrangement (not implementable). (b) Tandem device of polymer–small-molecule arrangement (can be implemented)

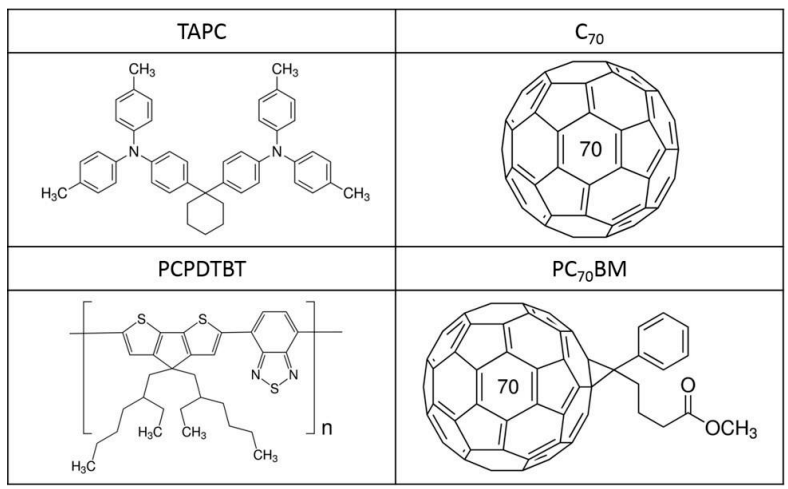

Figure 3.2 Chemical structure of active layer materials.

3.2 The structure and fabrication process of hybrid organic tandem solar cells

Figure 3.3a shows a structure of hybrid organic tandem solar cells fabricated in this study comprising: glass/185 nm indium tin oxide (ITO)/2 nm MoO_3 /TAPC:C_{70} /3 nm 3,4,9,10-perylenetetracarboxylic bisimidazole (PTCBI):C_{70} /4 nm PTCBI/0.1 nm Ag/10 nm hexaazatriphenylene-hexacarbonitrile (HAT-CN)/90 nm PCPDTBT:$PC_{70}BM$/20 nm Ca/100 nm Al. All organic materials were purchased and used without further purification. PCPDTBT and $PC_{70}BM$ were purchased from 1-material, Inc. and Nano-C, Inc., respectively. C_{70} and TAPC were purchased from Lumtec, while HAT-CN and PTCBI were purchased from Jilin OLED Material Technology.

The absorption coefficients of TAPC:C_{70} and PCPDTBT: $PC_{70}BM$ films determined by spectroscopic ellipsometry (Fig. 3.3b and Fig. 3.4) show that both layers are absorptive in the spectral region with wavelength λ less than 650 nm, while appreciable absorption of photons with $\lambda > 700$ nm can occur only in the PCPDTBT:$PC_{70}BM$. Since the values for V_{OC} of typical TAPC:C_{70} based single-junction devices are ~ 0.85 V [14], which is larger than those of PCPDTBT:$PC_{70}BM$ single-junction devices [29] (V_{OC} ~ 0.60 V), in an optimized tandem cell where the thermalization loss is minimized, absorption of the shorter-wavelength photons ($\lambda < 650$ nm) must occur in the TAPC:C_{70}.

Therefore, the TAPC:C_{70} was chosen as the absorption layer of the bottom subcell, requiring that the PCPDTBT:$PC_{70}BM$ absorption layer of the top subcell must be deposited without degrading the underlying small molecule layers. The PTCBI/Ag/HAT-CN trilayer is the interconnection layer (ICL) electrically connecting the two subcells: electrons photogenerated in the bottom subcell are transported through the PTCBI to recombine in the Ag islands with photogenerated holes transported from the top subcell through the HAT-CN layer. The PTCBI:C_{70} buffer layer was inserted between the TAPC:C_{70} and PTCBI layers to facilitate electron transport and thus increase the fill factor (FF) [30].

The fabrication process of the hybrid organic tandem solar cell by the thin-film transfer technique is schematically illustrated in Fig. 3.5. First, a PCPDTBT:$PC_{70}BM$ solution, prepared by mixing PCPDTBT and $PC_{70}BM$ in chlorobenzene (CB) with a 1,8-diiodooctane (DIO) additive, is spin-coated on a UV-ozone treated elastomeric stamp made of poly(dimethylsiloxane) (PDMS) (Fig. 3.5a). Immediately following the spin-coating, the PDMS stamp is stored in high vacuum (~10^{-7} Torr) for 1.5 h to remove the DIO additive, which is required to obtain a bulk heterojunction (BHJ) morphology with a high internal quantum efficiency (IQE) [31]. The immediate removal of the additive is also found to be crucial for successful transfer of the

PCPDTBT:$PC_{70}BM$ BHJ layer onto the bottom subcell, since a slower drying process, such as commonly used solvent annealing [32], causes the PDMS stamp to swell, which leads to diffusion of PCPDTBT:$PC_{70}BM$ into the stamp. In parallel, a small molecule-based bottom subcell is prepared by sequentially depositing MoO_3, TAPC:C_{70}, and PTCBI:C_{70} layers on a UV-ozone treated ITO-coated glass substrate by thermal evaporation in vacuum, followed by deposition of the ICL consisting of PTCBI/Ag/HAT-CN, also by thermal evaporation in vacuum (Fig. 3.5b). Next, the stamp is pressed onto the substrate with mild heating (Fig. 3.5c), and the PCPDTBT:$PC_{70}BM$ film is transferred onto the ICL as the stamp is peeled off from the substrate (Fig. 3.5d). Deposition of the top electrode composed of Ca/Al through a shadow mask by thermal evaporation in vacuum completes the fabrication of the hybrid organic tandem solar cell (Fig. 3.5e). In general, an optimal BHJ morphology of a polymer:fullerene derivative layer is formed by inducing an appropriate degree of phase separation between the constituent materials [33]. Since the phase separation process depends critically on experimental variables such as spin-coating speed, fullerene derivative concentration, and solvent evaporation rate [33], a BHJ morphology with a high IQE is difficult to obtain over a broad range of thicknesses [29]. Therefore, the thickness of the PCPDTBT:$PC_{70}BM$ layer was fixed at 90 nm, where a processing

condition described in the Method Section yields a BHJ layer with a high IQE. In contrast, since varying the layer thickness without significantly affecting the BHJ morphology is relatively easier for a vacuum-deposited TAPC:C_{70} film, the thickness of that layer *t* was varied so that four sets of tandem devices with *t* = 90, 120, 160, and 200 nm, respectively, were fabricated. In addition, a hybrid organic tandem solar cell where its PCPDTBT:$PC_{70}BM$ layer was deposited by spin-coating, instead of thin-film transfer, and where all other layers were identical to the corresponding layers in the transfer-fabricated devices was prepared for comparison. All devices were fabricated on ITO-coated glass substrates (15 Ω/sq., 25 mm by 25 mm), which were sequentially cleaned with detergent, de-ionized water, acetone, and isopropyl alcohol, followed by baking at 200 °C for 10 min in a vacuum oven prior to film depositions. All layers except the PCPDTBT:$PC_{70}BM$ were deposited by thermal evaporation in vacuum (~10^{-7} Torr). Deposition rates were ~1 Å/s except for the 0.1-nm-thick Ag "layer" in the ICL and the Ca layer in the top electrodes, whose deposition rates were 0.1 Å/s and 0.2 Å/s, respectively. The TAPC:C_{70} layers were formed by doping C_{70} layers with TAPC at 5 wt.% by co-evaporation. Also, the PTCBI:C_{70} layers were deposited by co-evaporating PTCBI and C_{70} in a volume ratio of 1:1. Device areas were defined by patterning of top metallic electrodes achieved by metal evaporation through

shadow masks with 2-mm-diameter circular openings. The PCPDTBT:$PC_{70}BM$ solution was prepared by dissolving 7.5 mg of PCPDTBT and 26.9 mg of $PC_{70}BM$ into a mixture of 0.03 ml DIO and 0.97 ml CB, with a magnetic stirring bar at 70 °C for 6 h [17] , and was spin coated at 2000 rpm for 20 s to obtain 90-nm-thick PCPDTBT:$PC_{70}BM$ layers on PDMS stamps. PDMS stamps were prepared by following a process described elsewhere. Pressing of PCPDTBT:$PC_{70}BM$-coated PDMS stamps onto substrates to transfer PCPDTBT:$PC_{70}BM$ films onto HAT-CN layers for fabrication of the tandem and single-junction devices was performed using a custom-built apparatus in an N_2 glove box, as described elsewhere [12]. To ensure that a conformal, intimate contact at the PCPDTBT:$PC_{70}BM$–HAT-CN interface was obtained throughout the substrate area, a pressure of 21.7 kgf/cm^2 was applied for 3 min while heating the samples at 100 °C.

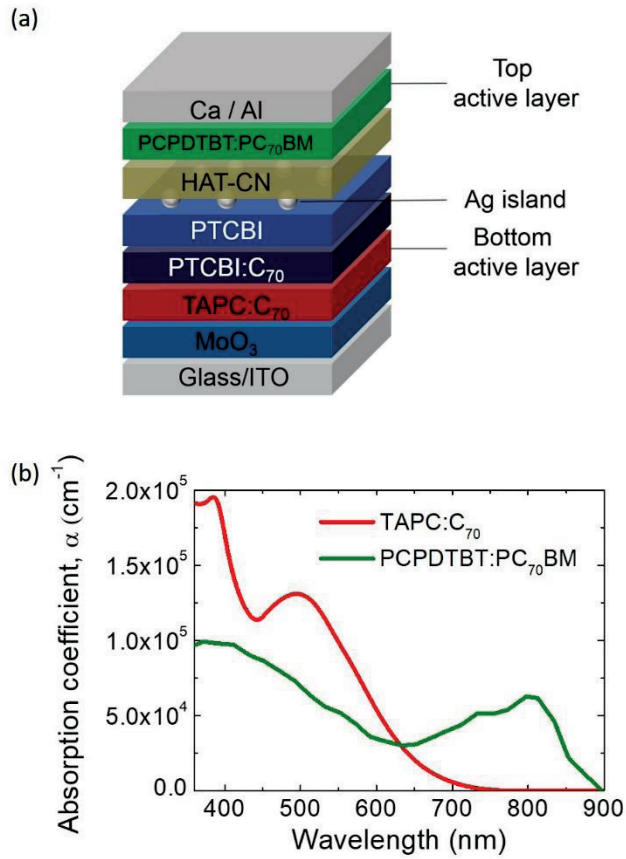

Figure 3.3 Device structure of transfer-fabricated tandem cells and absorption coefficients of active layers. (a) Device structure of a transfer-fabricated tandem cell whose top and bottom subcells have active layers composed of PCPDTBT:$PC_{70}BM$ and TAPC:C_{70} (b) Absorption coefficients of PCPDTBT:$PC_{70}BM$ (green) and TAPC:C_{70} (red) determined by spectroscopic ellipsometry.

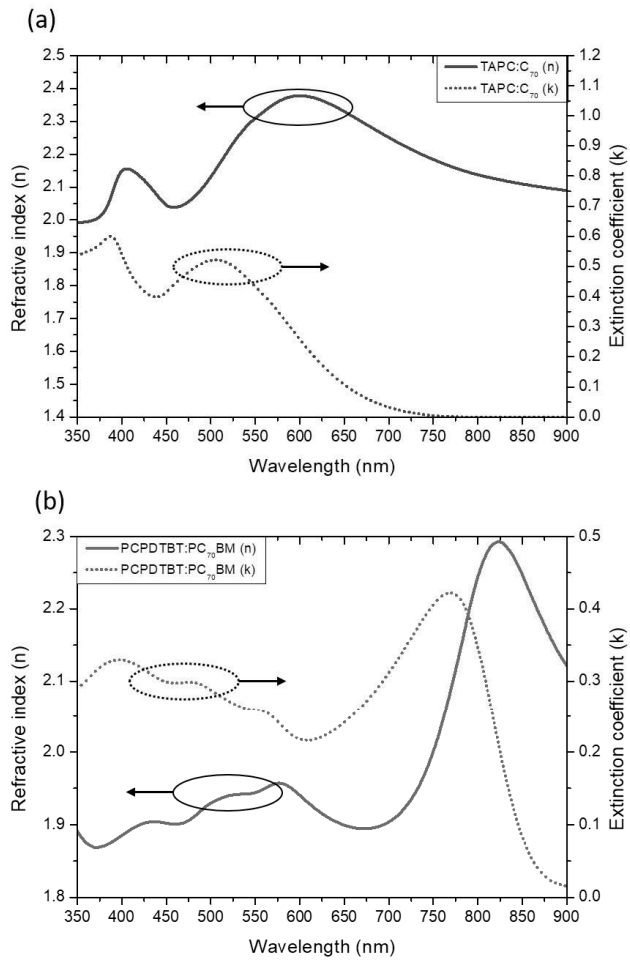

Figure 3.4 Refractive index (solid lines) and extinction coefficient (dotted lines) of (a) TAPC:C_{70} and (b) PCPDTBT:PC_{70}BM layers.

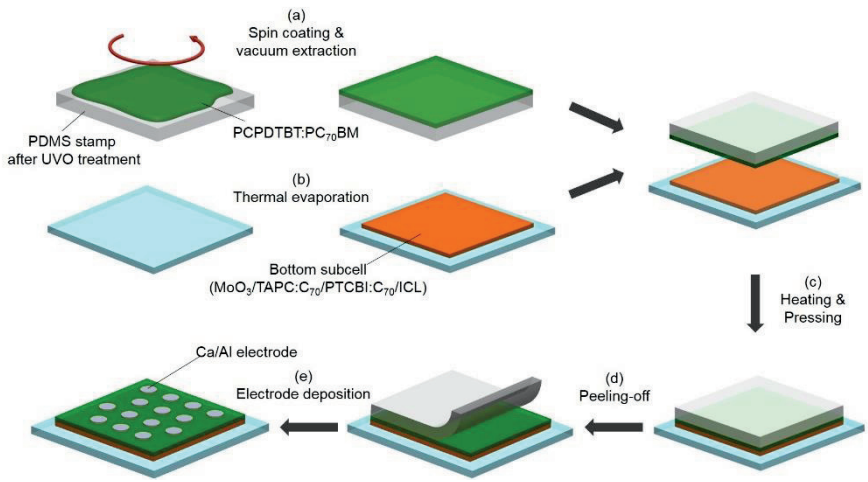

Figure 3.5 Schematic illustration of fabrication of hybrid organic tandem solar cells by the thin-film transfer technique. (a) Spin-coating of a PCPDTBT:$PC_{70}BM$ solution on a PDMS stamp and removal of a solvent and an additive. (b) Bottom subcell deposition on an ITO-coated glass substrate by thermal evaporation in vacuum. (c) Pressing of the stamp on the substrate with mild heating. (d) Peeling off the PDMS stamp from the substrate. (e) Deposition of the top electrodes.

3.3 Electrical characteristics of hybrid organic tandem solar cells

Figure 3.6a shows the current density versus voltage (*J–V*) characteristics of the hybrid organic tandem solar cells with different *t*, whose PCPDTBT:$PC_{70}BM$ layer was deposited by thin-film transfer, measured under simulated 1 sun AM 1.5 G illumination. The *J–V* characteristics were measured using a source meter (2400, Keithley) and a solar simulator (PEC-L01, Peccell Technologies) calibrated with a standard silicon solar cell (BS-520BK, Bunkoukeiki). The device parameters, such as V_{OC}, short-circuit current density (J_{SC}), FF, and PCE, are listed in Table 2. As *t* increases from 90 to 120 nm, J_{SC} increases from 8.04 to 8.48 mA cm^{-2}, and a further increase in *t* decreases J_{SC}. This result indicates, as discussed later more quantitatively, that (i) at *t* = 90 nm, J_{SC} of the tandem cell is limited by insufficient optical absorption in the bottom subcell, (ii) near *t* = 120 nm, the currents generated in both subcells are matched to each other, thereby maximizing J_{SC} of the tandem device, and (iii) *t* > ~120 nm is optically too thick, meaning that the bottom subcell absorbs too many photons so that J_{SC} of the tandem cell is limited by the top subcell. As a result of the short-circuit current matching, the device with *t* = 120 nm (red circles) has the highest J_{SC} of 8.48 mA cm^{-2}, with V_{OC} = 1.46 V and FF = 0.51, leading to the highest PCE of 6.26%. To the best

of my knowledge, this is the highest PCE among small molecule–polymer hybrid organic tandem solar cells reported so far [22,33,34]. The device with t = 200 nm (green circles) suffers not only from a large imbalance between the subcell currents but also from a substantially decreased FF arising from increased series resistance. Consequently, it has the lowest PCE of 1.99%. Figure 3.5b compares the *J–V* curve of the tandem device with the highest PCE (the device with t = 120 nm, blue circles) with that of a single-junction device whose active layer is TAPC:C_{70} (red triangles) or PCPDTBT:$PC_{70}BM$ (green squares). The structures of the single-junction devices are: glass/185 nm ITO/2 nm MoO_3 /120 nm TAPC:C_{70} /3 nm PTCBI:C_{70} /4 nm PTCBI/100 nm Ag, and glass/185 nm ITO/10 nm HAT-CN/90 nm PCPDTBT:$PC_{70}BM$/20 nm Ca/100 nm Al. The value of V_{OC} for the tandem cell (1.46 V) is almost identical to the sum of V_{OC} values for single-junction devices (1.48 V), indicating that holes photogenerated in the top subcell are readily transported across the PCPDTBT:$PC_{70}BM$–HAT-CN interface formed by thin-film transfer and recombine with electrons transported from the bottom subcell. Also shown in Fig. 3.6b is the *J–V* curve of a tandem device whose device structure was identical to that of the transfer-fabricated tandem device, except for its PCPDTBT:$PC_{70}BM$ layer deposited by spin-coating, instead of thin-film transfer (dotted line). For the spin-coated device, V_{OC} is significantly

decreased to 0.51 V, indicating that the series connection between the top and bottom subcells was not properly made in this case.

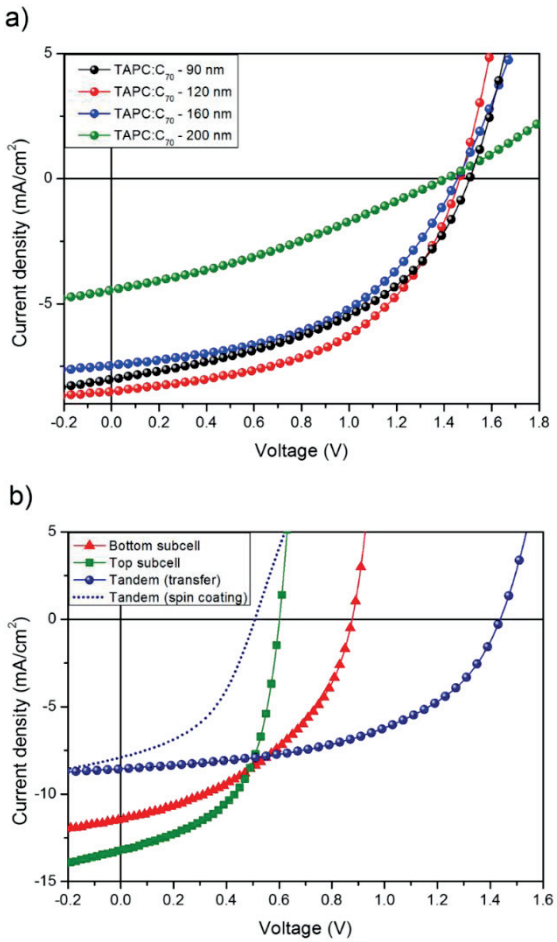

Figure 3.6 Current density vs voltage (*J–V*) characteristics of single-junction and tandem solar cells. (a) *J–V* characteristics of transfer-fabricated organic tandem solar cells with varying TAPC:C_{70} thickness. (b) *J–V* characteristics of transfer-fabricated and spin-coated tandem cells with 120-nm-thick TAPC:C_{70} layers, and two single-junction cells whose active layers are TAPC:C_{70} and PCPDTBT:$PC_{70}BM$, respectively.

3.4 Differences in hybrid tandem solar cells fabricated by spin-coating and thin-film transfer

In Fig. 3.7, the cross-sectional TEM images of the transfer-fabricated hybrid organic tandem solar cell are compared with those of the spin-coated device. The cross-sectional images of the spin-coated and transfer-fabricated tandem solar cells were obtained using a TEM (JEM-2100F, JEOL) and the samples for the TEM measurements were prepared using a focused ion beam instrument (Quanta 3D FEG, FEI). In the case of the spin-coated device, the total thickness of the layers between the two electrodes, which are supposed to be the small molecule layers for the bottom subcell, the ICL layer, and the PCPDTBT:$PC_{70}BM$ layer, is found to be ~90 nm, as indicated by an arrow in Fig. 3.7a. This is much smaller than the designed value of 230 nm: the spin-coating condition was the same as that used to obtain 90-nm-thick PCPDTBT:$PC_{70}BM$ films on PDMS stamps in Fig. 3.5a. As expected, this result is due to the penetration of the solvent through the ICL and the bottom subcell, and the resulting intermixing of the constituent layers, leading to a very poor device performance as shown in Fig. 3.7a and Table 2. In contrast, in the transfer-fabricated device, the total thickness of the tandem device was unchanged from the designed value, with the transfer-fabricated PCPDTBT:$PC_{70}BM$ (i) and thermally evaporated small molecule (ii) layers

marked by arrows in Fig. 3.6b, which implies that the small molecule layers were not damaged by the thin-film transfer process. Furthermore, the morphological quality of the HAT-CN–PCPDTBT:$PC_{70}BM$ interface formed by thin-film transfer is remarkably high so that it cannot be identified even in a high-resolution image (Fig. 3.7c) of the area enclosed by a black square in Fig. 3.7b. This is in line with our previous report where a MoO_3–polymer:fullerene interface that is void-free at the nanoscale has been formed by transferring the polymer:fullerene layer onto the MoO_3 layer [27]. Figure 3.7d is a high-resolution image of the area in Fig. 3.7b enclosed by a red square, showing voids (iii) and a region (iv) that is brighter than the surrounding. These features were determined to have been generated by damage incurred during focused-ion beam milling used in sample preparation [35], since the *J–V* curve with characteristics typical of a tandem device with the good electrical connection between the subcells, as shown in Fig. 3.6, cannot be expected, if the features, which are observed in large areas at the interface as shown in Fig. 3.7b, had been caused by the thin-film transfer process and therefore had been present in the device before the *J–V* measurement. It may be argued that the good *J–V* characteristic shown in Fig. 3.6 can still be obtained in the presence of the features if photogenerated electrons and holes migrate to void-free regions to recombine with each other.

This possibility, however, is ruled out since the lateral dimensions of the regions with the features are comparable to the thickness of the device (Fig. 3.7b), and therefore a non-negligible loss in voltage or current must have been observed if they had not been caused by damage from the focused-ion beam process.

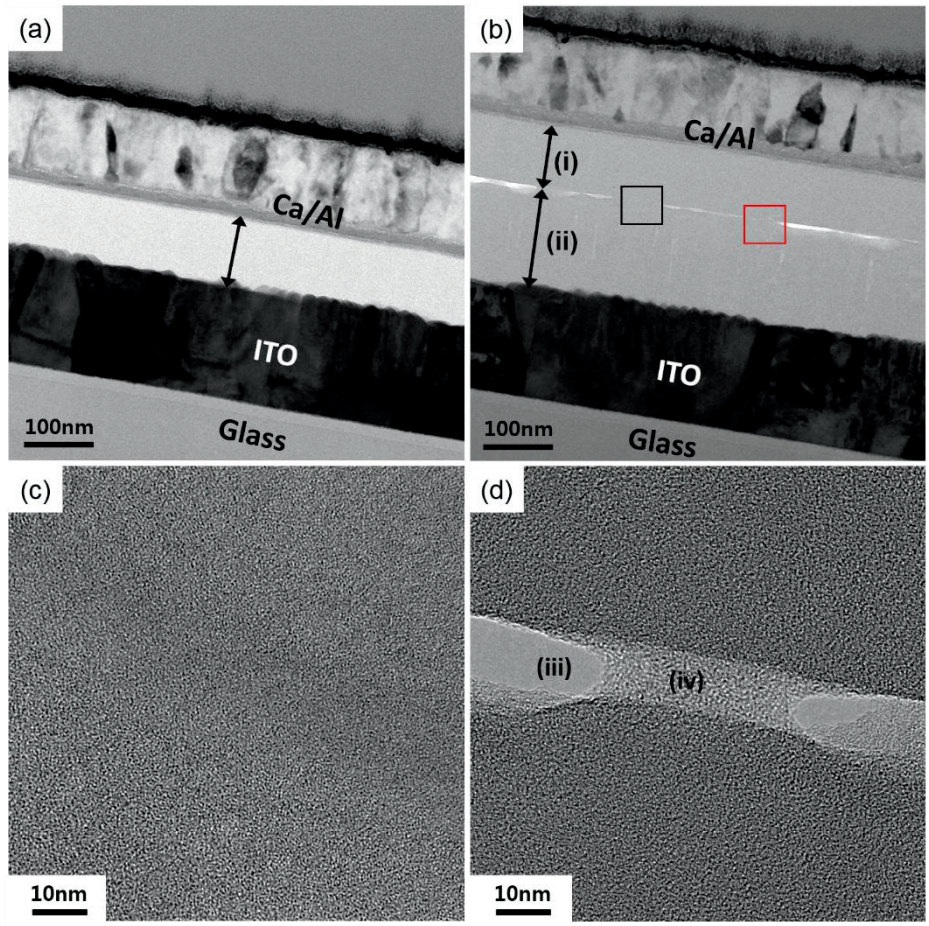

Figure 3.7 Cross-sectional transmission electron microscope (TEM) images of hybrid organic tandem solar cells. Cross-sectional TEM image of (a) spin-coated and (b–d) transfer-fabricated tandem solar cells. (c) and (d) are the images of the regions enclosed by black and red squares in (b), respectively. For the transfer-fabricated device, thicknesses of the transferred PCPDTBT:$PC_{70}BM$ layer (i) and the thermally evaporated small-molecule layers (ii) were unchanged from the designed values. The features (iii) and (iv) in (d) were generated during focused-ion beam milling used in sample preparation.

Table 2 Photovoltaic parameters of hybrid organic tandem solar cells with different thicknesses of the bottom active layer (TAPC:C_{70}) and single-junction cells whose active layers are TAPC:C_{70} or PCPDTBT:$PC_{70}BM$.

	TAPC:C_{70} Thickness (nm)	**J_{SC} (mA cm^{-2})**	**V_{OC} (V)**	**FF**	**PCE (%)**
Single-junction cell (TAPC:C_{70})	120	11.6	0.89	0.42	4.39
Single-junction cell (PCPDTBT:$PC_{70}BM$)	·	13.2	0.59	0.55	4.26
Tandem cell (transfer-fabricated)	90	8.04	1.5	0.46	5.49
	120	8.48	1.46	0.51	6.26
	160	7.44	1.45	0.48	5.22
	200	4.45	1.4	0.32	1.99
Tandem cell (spin-coated)	120	7.9	0.51	0.45	1.82

3.5 Quantitative analysis of the hybrid organic tandem solar cell using numerical simulations

The dependency of J_{SC} of the transfer-fabricated device on t, summarized in Table 2, can be quantitatively explained by numerical simulations. To obtain simulated J_{SC}, I first calculated the optical absorption efficiency of each active layer – the probability that a photon incident on the tandem cell is absorbed in that active layer – using the transfer-matrix method [36]. Next, for simplicity both subcells were assumed to have a common, wavelength-independent IQE that does not vary with the active layer thicknesses. The EQE of each active layer – the probability that a photon incident on the tandem cell leads to separated charge carriers resulting from absorption in that active layer – was then given by the product of its absorption efficiency and IQE. The solar-spectrum-weighted integral of EQE of each active layer yielded the photocurrent density of each subcell, the smaller of which was taken as an estimate of J_{SC} of the tandem cell. Figure 3.8 shows the experimental (circle) and simulated (line) values of J_{SC} as a function of t, where the IQE, regarded as a fitting parameter, was determined to be 0.76 to minimize the total error between the experiment and simulation for t = 90, 120, and 160 nm. The data point at t = 200 nm was excluded in the fitting, since a decrease in IQE due to poor charge collection is often observed for a thick BHJ layer [37−39]. Except

for t = 200 nm, at which the IQE is expected to be smaller than 0.76, the three data points are well fit by the simulation. In particular, the location of the maximum J_{SC} for the simulated case agrees well with that for the experiment, meaning that my simulation – although not useful in accurately predicting the actual values of J_{SC} due to assumptions made for simplicity – can be used as a simple yet effective guideline for maximizing J_{SC} of transfer-fabricated tandem solar cells. The inset of Fig. 3.8 shows that at t = 120 nm the photocurrents of the top (solid line) and bottom (dotted line) subcells are matched, maximizing J_{SC}, and that as t increases (or decreases) from 120 nm, J_{SC} is limited by insufficient absorption in the top (or bottom) subcell.

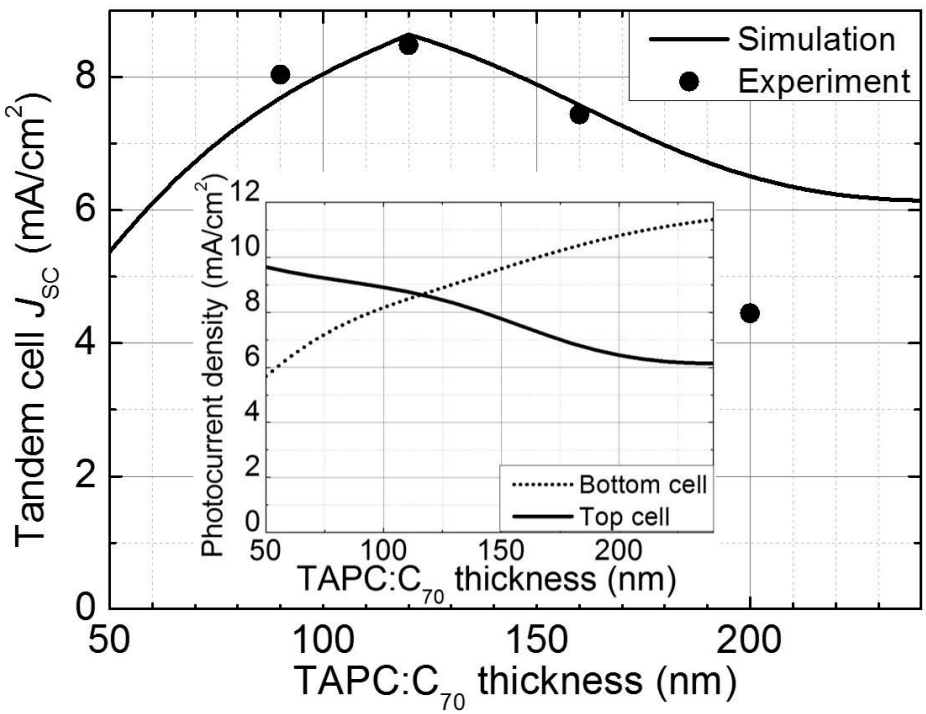

Figure 3.8 Calculated and measured short-circuit current densities (J_{SC}) of the transfer-fabricated tandem devices with different TAPC:C_{70} thicknesses (t). The calculated (line) and measured (circle) values of J_{SC} for the transfer-fabricated tandem device shown in Fig. 3.3 as functions of t. The inset shows the photocurrent densities of the top (solid line) and bottom (dotted line) subcells as functions of t.

3.6 Conclusion

I have fabricated small molecule–polymer hybrid organic tandem solar cells whose active layers are based on PCPDTBT:$PC_{70}BM$ and TAPC:C_{70}. By examining optical absorption spectra of both layers and values of V_{OC} expected from these donor–acceptor pairs, the PCPDTBT:$PC_{70}BM$- and TAPC:C_{70} -based subcells were determined to be located at the top and bottom, respectively, to maximize the PCE. This device configuration makes inapplicable the conventional spin-coating method for polymer deposition, due to damage to the underlying small molecule layers by a liquid solvent used in spin-coating. I, therefore, have employed a solvent-free method where a PCPDTBT:$PC_{70}BM$ layer deposited on an elastomeric stamp is transferred onto a small molecule bottom subcell. Cross-sectional TEM images show that the interface between PCPDTBT:$PC_{70}BM$ and small molecule layers formed by thin-film transfer is remarkably intimate, leading to V_{OC} of the tandem device almost equaling the sum of V_{OC} of the two subcells. A tandem device optimized by varying the thickness of the TAPC:C_{70} layer has J_{SC} = 8.48 mA cm^{-2} and PCE = 6.26%, the latter being one of the highest among small molecule–polymer hybrid tandem solar cells. Since the thin-film transfer technique allows for the maximal utilization of materials choice that small molecules and polymers offer in combination, with further efforts, it may

potentially realize commercially viable, highly efficient small molecule–polymer tandem solar cells.

3.7 References

[1] S. Günes, H. Neugebauer, N. S. Sariciftci, Conjugated polymers for organic solar cells. Chem. Rev., 107 (2007) 1324–1338.

[2] H. Hoppea, N. S. Sariciftci, Organic solar cells: an overview. J. Mater. Res., 19 (2004) 1924–1945.

[3] G. Li, R. Zhu, Y. Yang, Polymer solar cells. Nat. Photon., 6 (2012) 153–161.

[4] L.-M. Chen, Z. Hong, G. Li, Y. Yang, Recent progress in polymer solar cells: manipulation of polymer:fullerene morphology and the formation of efficient inverted polymer solar cells. Adv. Mater., 21 (2009) 1434–1449.

[5] K. L. Chopra, P. D. Paulson, V. Dutta, Thin-film solar cells: an overview. Prog. Photovolt: Res. Appl., 12, (2004) 69–92.

[6] Y. Li, Molecular design of photovoltaic materials for polymer solar cells: toward suitable electronic energy levels and broad absorption. Acc. Chem. Res., 45, (2012) 723–733.

[7] A. W. Hains, Z. Liang, M. A. Woodhouse, B. A. Gregg, Molecular semiconductors in organic photovoltaic cells. Chem. Rev., 110 (2010) 6689–6735.

[8] Y. J. Cheng, S. H. Yang, C. S. Hsu, Synthesis of conjugated polymers for organic solar cell applications. Chem. Rev., 109 (2009) 5868–5923.

[9] J. N. Munday, H. A. Atwater, Large integrated absorption enhancement in plasmonic solar cells by combining metallic gratings and antireflection coatings. Nano Lett., 11 (2011) 2195–2201.

[10] R. Biswas, E. Timmons, Nano-photonic light trapping near the Lambertian limit in organic solar cell architectures. Opt. Express, 21 (2013) A841–A846.

[11] C. Girotto, D. Moia, B. P. Rand, P. Heremans, High-performance organic solar cells with spray-coated hole-transport and active layers. Adv. Funct. Mater. 21 (2010) 64–72.

[12] D. H. Wang, D.-G. Choi, K.-J. Lee, O O. Park, J. H. Park, Photovoltaic devices with an active layer from a stamping transfer technique: single layer versus double layer. Langmuir, 26 (2010) 9584–9588.

[13] G. Dennler, K. Forberich, T. Ameri, C. Waldauf, P. Denk, C. J. Brabec, K. Hingerl, A. J. Heeger, Design of efficient organic tandem cells: on the interplay between molecular absorption and layer sequence. J. Appl. Phys.,102 (2007) 123109-1–123109-6.

[14] Y. Gao, F. Jin, W. Li, Z. Su, B. Chu, J. Wang, H. Zhao, H. Wu, C. Liu, F. Hou, T. Lin, Q. Song, Highly efficient organic tandem solar cell with a SubPc interlayer based on TAPC:C70 bulk heterojunction. Sci. Rep., 6 (2016) 1–8.

[15] J. You, L. Dou, K. Yoshimura, T. Kato, K. Ohya, T. Moriarty, K. Emery,

C-. C. Chen, J. Gao, G. Li, Y. Yang, A polymer tandem solar cell with 10.6% power conversion efficiency. Nat. Commun., 4 (2013) 1446–1410.

[16] L. Dou, J. You, J. Yang, C.-C. Chen, Y. He, S. Murase, T. Moriarty, K. Emery, G. Li, Y. Yang, Tandem polymer solar cells featuring a spectrally matched low-bandgap polymer. Nat. Photon., 6 (2012) 180–185.

[17] J. Y. Kim, K. Lee, N. E. Coates, D. Moses, T.-Q. Nguyen, M. Dante, A. J. Heeger, Efficient tandem polymer solar cells fabricated by all-solution processing. Science, 317 (2007) 222–225.

[18] N. Li, C. J. Brabec, Air-processed polymer tandem solar cells with power conversion efficiency exceeding 10%. Energy Environ. Sci., 8 (2015) 2902–2909.

[19] J. You, L. Dou, Z. Hong, G. Li, Y. Yang, Recent trends in polymer tandem solar cells research. Prog. Polym. Sci., 38 (2013) 1909–1928.

[20] H.-S. Shim, J.-H. Chang, C.-I. Wu, J.-J. Kim, Effect of different p-dopants in an interconnection unit on the performance of tandem organic solar cells. Org. Electron., 15 (2014) 1805–1809.

[21] H.-S. Shim, S.-Y. Kim, J. W. Kim, T.-M. Kim, C.-H. Lee, J.-J. Kim, An efficient interconnection unit composed of electron-transporting layer/metal/p-doped hole-transporting layer for tandem organic photovoltaics. Appl. Phys. Lett., 102 (2013) 203903-1–203903-4.

[22] A. Colsmann, J. Junge, C. Kayser, U. Lemmer, Organic tandem solar cells comprising polymer and small-molecule subcells. Appl. Phys. Lett. 89 (2006) 203506-1–203506-3.

[23] Heliatek, http://www.heliatek.com/en/press/press-releases/details/heliatek-consolidates-its-technology-leadership-by-establishing-a-new-world-record-for-organic-solar-technology-with-a-cell-effi (2013).

[24] S. Sista, Z. Hong, L.-M. Chen, Y. Yang, Tandem polymer photovoltaic cells – current status, challenges and future outlook. Energy Environ. Sci., 4 (2011) 1606–1620.

[25] G. Dennler, M. C. Scharber, T. Ameri, P. Denk, K. Forberich, C. Waldauf, C. J. Brabec, Design rules for donors in bulk-heterojunction tandem solar cells: towards 15% energy-conversion efficiency. Adv. Mater., 20 (2008) 579–583.

[26] W. Huang, E. Gann, L. Thomsen, A. Tadich, Y-. B. Cheng, C. R. McNeill, Metal Evaporation-induced degradation of fullerene acceptors in polymer/fullerene solar cells. ACS Appl. Mater. Interfaces, 8 (2016) 2247–2254.

[27] E. Lee, J. Kim, C. Kim, Polymer tandem photovoltaic cells with molecularly intimate interfaces achieved by a thin-film transfer technique. Sol. Energ. Mat. Sol. Cells, 105 (2012) 1–5.

[28] M. A. Meitl, Z.-T. Zhu, V. Kumar, K. J. Lee, X. Feng, Y. Y. Huang, I.

Adesida, R. G. Nuzzo, J. A. Rogers, Transfer printing by kinetic control of adhesion to an elastomeric stamp. Nat. Mater., 5 (2005) 33–38.

[29] S. Albrecht, S. Schäfer, I. Lange, S. Yilmaz, I. Dumsch, S. Allard, U. Scherf, A. Hertwig, D. Neher, Light management in PCPDTBT:PC70BM solar cells: a comparison of standard and inverted device structures. Org. Electron., 13 (2012) 615–622.

[30] H.-S. Shim, F. Lin, J. Kim, B. Sim, T.-M. Kim, C.-K. Moon, C.-K. Wang, Y. Seo, K.-T. Wong, J.-J. Kim, Efficient vacuum-deposited tandem organic solar cells with fill factors higher than single-junction subcells. Adv. Energy Mater., 5 (2015) 1500228-1–1500228-7.

[31] A. Zusan, B. Gieseking, M. Zerson, V. Dyakonov, R. Magerle, C. Deibel, The effect of diiodooctane on the charge carrier generation in organic solar cells based on the copolymer PBDTTT-C. Sci. Rep., 5 (2015) 8286-1–8286-8.

[32] A. J. Moulé, K. Meerholz, Controlling morphology in polymer-fullerene mixtures. Adv. Mater., 20 (2008) 240–245.

[33] A. G. F. Janssen, T. Riedl, S. Hamwi, H.-H. Johannes, W. Kowalsky, Highly efficient organic tandem solar cells using an improved connecting architecture. Appl. Phys. Lett., 91 (2007) 073519-1–073519-3.

[34] G. Dennler, H-. J. Prall, R. Koeppe, M. Egginger, R. Autengruber, N. S. Sariciftci, Enhanced spectral coverage in tandem organic solar cells. Appl.

Phys. Lett., 89 (2006) 073502-1–073502-3.

[35] S. Kim, M. J. Park, N. P. Balsara, G. Liu, A. M. Minor, Minimization of focused ion beam damage in nanostructured polymer thin films. Ultramicroscopy, 111 (2011) 191–199.

[36] L. A. A. Pettersson, L. S. Roman, O. Inganas, Modeling photocurrent action spectra of photovoltaic devices based on organic thin films. J. Appl. Phys., 86 (1999) 487–496.

[37] L. H. Slooff, S. C. Veenstra, J. M. Kroon, D. J. D. Moet, J. Sweelssen, M. M. Koetse, Determining the internal quantum efficiency of highly efficient polymer solar cells through optical modeling. Appl. Phys. Lett., 90 (2007) 143506-1–143506-3.

[38] G. Burkhar, E. Hoke, S. Scully, M. McGehee, Incomplete exciton harvesting from fullerenes in bulk heterojunction solar cells. Nano Lett., 9 (2009) 4037–4041.

[39]. G. Li, V. Shrotriya, Y. Yao, Y. Yang, Investigation of annealing effects and film thickness dependence of polymer solar cells based on poly(3-hexylthiophene). J. Appl. Phys., 98 (2005) 043704-1–043704-5.

Chapter 4 Polymer tandem solar cells with new interconnection layer using dry thin-film transfer printing

4.1 Overview

Although organic solar cells have the potential for a low-cost, lightweight, and flexible energy conversion device [1,2], they have not yet been commercialized because of their low efficiency. The efficiency of organic solar cells can be improved by fabricating a tandem device consisting of stacked active layers with complementary absorption spectra to widen the optical absorption range and minimize the thermalization loss [3,4].

An interconnection layer (ICL) that electrically connects the constituent subcells is a crucial element in a tandem solar cell, which in general must meet the following criteria: it must add the photovoltages of the adjacent subcells with minimal loss and have negligible optical absorption. For polymer tandem solar cells, whose active layers are typically deposited by liquid phase processes such as spin-coating [4], ink-jet printing [5], and spray coating [6], ICLs must also block the penetration of the solvent used for depositing the active layer of the top subcell, to prevent damage and/or dissolution of the bottom subcell.

As a result, the types of ICLs used in polymer tandem devices have so far been limited, with the most commonly used ICL being that composed of poly(3,4-ethylenedioxythiophene):poly (styrenesulfonate) (PEDOT:PSS) / metal oxide, such as PEDOT:PSS/ZnO [7,8] and PEDOT:PSS/TiO_x [9], where PEDOT:PSS is used as a hole transport layer (HTL) and solvent blocking layer and the metal oxides are used as an electron transport layer (ETL). Although tandem cells featuring these ICLs have good performances, with the open-circuit voltages (V_{OC}) similar to the sum of V_{OC} of the subcells, PEDOT:PSS is not an ideal material to use for ICLs for the following reasons: its acidic nature may decrease the device lifetime [10], and it absorbs light in the visible and near-infrared spectral regions, resulting in an optical loss [11]. Therefore, efforts have been made to replace PEDOT:PSS with a p-type metal oxide, such as nickel oxide (NiO_x) [12,13], molybdenum trioxide (MoO_3) [14], vanadium pentoxide (V_2O_5) [14], and tungsten trioxide (WO_3) [15]. Thin films composed of these materials, however, tend to have small degrees of porosity, and thus, the complete prevention of solvent penetration has been difficult to achieve with an ICL composed of a metal oxide bilayer, whose thickness is typically less than 30 nm. Consequently, polymer tandem cells with a metal oxide ICL often have V_{OC} losses [16].

For small molecule tandem devices, because all the constituent layers are

deposited using vacuum thermal evaporation, the materials and structures of ICLs can be chosen without the restriction imposed by the solvent blocking requirement. Furthermore, the electrical properties required for avoiding a V_{OC} loss at the ICL, namely, efficient transport and recombination of charge carriers, can readily be achieved in vacuum thermal evaporation by precise control of layer thicknesses and/or electrical doping [17]. Thus, a variety of ICLs have been developed for small molecule tandem cells, such as HTL/metal/ETL [18] and doped HTL/doped ETL [19].

In this research, it was demonstrated that an ICL formed using vacuum thermal evaporation can be applied to a polymer tandem solar cell by depositing the light-absorbing layer of the top subcell using a dry thin-film transfer technique. Specifically, a polymer tandem cell was fabricated, whose top and bottom light-absorbing layers were: poly[2,6-(4,4-bis-(2-ethylhexyl)-4H-cyclopenta[2,1-b;3,4-b′]dithiophene)-alt-4,7-(2,1,3-benzothiadiazole)] (PCPDTBT):[6,6]-phenyl C_{70} -butyric acid methyl ester ($PC_{70}BM$) and poly(3-hexylthiophene) (P3HT): [6,6]-phenyl C_{60} -butyric acid methyl ester ($PC_{60}BM$), respectively. The cell was made by transfer printing the PCPDTBT:$PC_{70}BM$ and P3HT:$PC_{60}BM$ layers onto a vacuum deposited ICL and a 1,4,5,8,9,11-hexaazatriphenylene hexacarbonitrile (HAT-CN) layer, respectively, using the method previously reported [20,21]. The ICL was

composed of bathocuproine:silver/silver islands/HAT-CN (BCP:Ag/Ag islands/HAT-CN), and the thicknesses of the BCP:Ag and Ag island layers were precisely controlled to maximize the device performance. Consequently, the tandem device featuring the optimized ICL exhibited a V_{OC} of 1.20 V, which was equal to the sum of the subcells' V_{OC}s, with its fill factor (FF = 0.60) almost identical to the FFs of the subcells. The results of this research also provided qualitative explanations for the effects of thickness variations of the BCP:Ag and Ag island layers on the device performance. This work shows that the thin-film transfer technique allows the exploitation of the advantageous attributes of vacuum thermal evaporation — precise controllability of layer thicknesses and doping concentrations, and availability of various materials including small molecules, metals, and metal oxides – to form ICLs whose materials and structures are tailored for given light-absorbing layers of polymer tandem cells.

4.2 The structure and fabrication process of polymer tandem solar cells

The device structure of the polymer tandem solar cells and the chemical structures of its photoactive layer materials deposited by the dry thin-film transfer process using polydimethylsiloxane (PDMS) stamps are shown in Fig. 4.1a. The solar cells have the following structure: glass/185 nm indium tin oxide (ITO)/10 nm HAT-CN/～200 nm P3HT:$PC_{60}BM$/BCP:Ag/Ag islands/10 nm HAT-CN/～90 nm PCPDTBT:$PC_{70}BM$/20 nm calcium (Ca)/100 nm aluminum (Al). All the organic materials were purchased and used without further purification. Polymers (P3HT, PCPDTBT) and fullerene derivatives ($PC_{60}BM$, $PC_{70}BM$) were purchased from 1-Material, Inc. and Nano-C, Inc., respectively. BCP and HAT-CN were purchased from Jilin OLED Material Technology. The P3HT:$PC_{60}BM$ solution was prepared by dissolving P3HT and $PC_{60}BM$ (1:1 w/w) into 1,2-dichlorobenzene with a total concentration of 34 mg ml^{-1}, with magnetic stirring at 70 °C for 6 h. The PCPDTBT:$PC_{70}BM$ solution was prepared using the method in Chapter 3. To match the photocurrents of the top and bottom subcells, the thicknesses of the photoactive layers were chosen, using the optical calculation based on the transfer matrix method, to be ～200 nm and ～90 nm for the P3HT:$PC_{60}BM$ and the PCPDTBT:$PC_{70}BM$, respectively [22]. The absorption efficiencies of

each active layer were calculated using the transfer matrix method (Fig. 4.1b). To simplify the calculation, it is assumed that each light absorption layer has a constant internal quantum efficiency (IQE) value at all wavelengths (P3HT:$PC_{60}BM$ = 0.85, PCPDTBT:$PC_{70}BM$ = 0.75). Then, the external quantum efficiency (EQE) of the top and bottom subcells is calculated by multiplying the absorption efficiency by the IQE. The solar-spectrum-weighted integral of EQE of each active layer yielded the photocurrent density of each subcell, the smaller of which was taken as an estimate of short-circuit current density (J_{SC}) of the tandem cell. The J_{SC} of the tandem solar cell is calculated according to the thickness of the top and bottom active layers and the thickness of the active layer which maximizes the J_{SC} is determined as the thickness of the active layer of the optimized tandem solar cell. Photons with wavelengths (λ) $\leq$ 600 nm are mostly absorbed by the P3HT:$PC_{60}BM$ [the bottom photoactive layer (blue triangles)], whereas those with $\lambda \geq$ 650 nm are mostly absorbed by the PCPDTBT:$PC_{70}BM$ [the top photoactive layer (red triangles)]. As a result, the tandem device is capable of harvesting photons in a wide spectral range extending down to $\sim$850 nm. Green circles in Fig. 4.1b correspond to the calculated absorption efficiency of the tandem cell as a whole, which compares well with the measured absorption efficiency of the tandem device fabricated using the thin-film transfer technique (black squares).

The HAT-CN deposited on ITO modifies the work function of ITO to ～5.5 eV [23], which facilitates the collection of holes generated in the bottom photoactive layer. Electrons generated in the top photoactive layer are collected at the Ca/Al top metal electrode. The ICL composed of a BCP:Ag/Ag islands/HAT-CN multilayer, which has high transmittance in the absorption region of the top subcell (Fig. 4.2), electrically connects the two subcells without a voltage loss. The BCP:Ag works as an ETL, allowing electrons generated in the bottom subcell to move readily to the interface between the HAT-CN and PCPDTBT:$PC_{70}BM$ layers, where they recombine with holes generated in the PCPDTBT:$PC_{70}BM$ layer. Generally, electron transport in a BCP layer occurs through gap states formed by metal deposited on it, not through its lowest unoccupied molecular orbital (LUMO) level. Because these damage induced gap states were expected to be formed only near the BCP surface by deposition of Ag islands whose "thickness" is ～1 nm, the BCP layer was doped with coevaporated Ag, which has been shown to create the gap states throughout the BCP layer [24].

The fabrication process of the polymer tandem solar cell is illustrated schematically in Fig. 4.3, where the bottom and top photoactive layers, P3HT:$PC_{60}BM$ and PCPDTBT:$PC_{70}BM$, respectively, were both deposited using dry thin-film transfer on the HAT-CN layers without damaging the

underlying organic(s) (Fig. 4.3b and e, respectively). After a P3HT:$PC_{60}BM$ solution was spin-coated on an ultraviolet (UV)-ozone treated PDMS stamp, a P3HT:$PC_{60}BM$ film was formed by sequential applications of solvent- [25] and thermal-annealing processes. The P3HT:$PC_{60}BM$ film was then transfer printed (Fig. 4.3b and c), with mild pressure and heat, onto a HAT-CN layer deposited on an ITO-coated substrate (Fig. 4.3a). Next, layers of BCP:Ag, Ag islands, and HAT-CN were sequentially deposited using thermal evaporation under vacuum with deposition rates of 1 Å s^{-1}:0.05 Å s^{-1}, 0.1 Å s^{-1}, and 1 Å s^{-1}, respectively to form an ICL (Fig. 4.3d), onto which a PCPDTBT:$PC_{70}BM$ film was transferred from a PDMS stamp (Fig. 4.3e) [21]. Unlike the bottom active layer, before the thin-film transfer, the PCPDTBT:$PC_{70}BM$ layer spin-coated onto the PDMS stamp was quickly dried under a high vacuum ($\sim 10^{-7}$ Torr) to prevent the diffusion of the PCPDTBT:$PC_{70}BM$ into the PDMS that would otherwise swell because of 1,8-diiodooctane (DIO) used as an additive for the PCPDTBT:$PC_{70}BM$ solution. Also, the stamp was stored under a high vacuum for 1.5 h to thoroughly remove the DIO additive, which is known to form trap states in PCPDTBT:$PC_{70}BM$ [26]. Finally, a top cathode was formed using thermal evaporation of Ca, followed by Al (Fig. 4.3f).

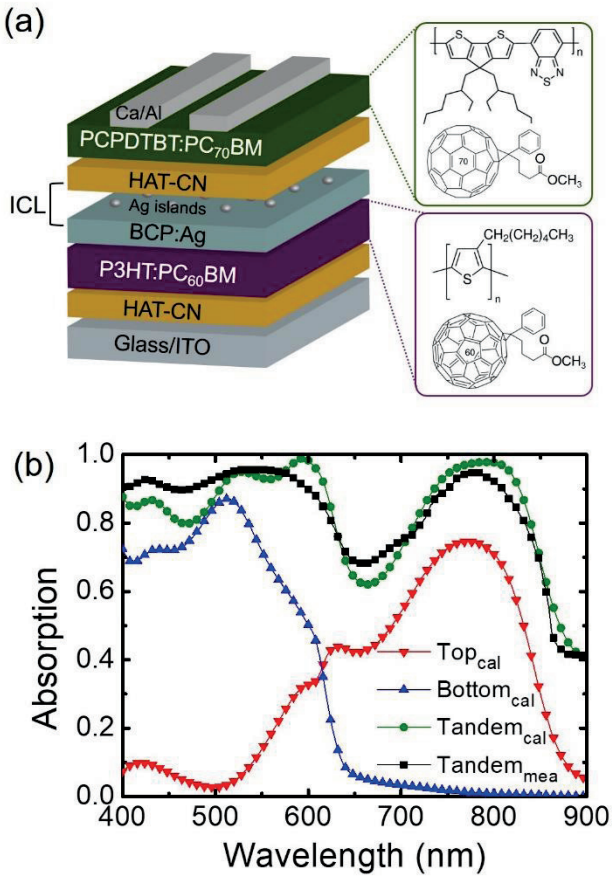

Figure 4.1 (a) Structure of the polymer tandem solar cells device fabricated using a thin-film transfer technique, and chemical structure of photoactive materials. (b) Spectra of the absorption efficiencies of the top (red) and bottom (blue) active layers calculated using the transfer matrix method. Also shown is the calculated absorption efficiency spectrum of the tandem device as a whole (green), compared with that measured for the tandem device fabricated using the thin-film transfer technique (black).

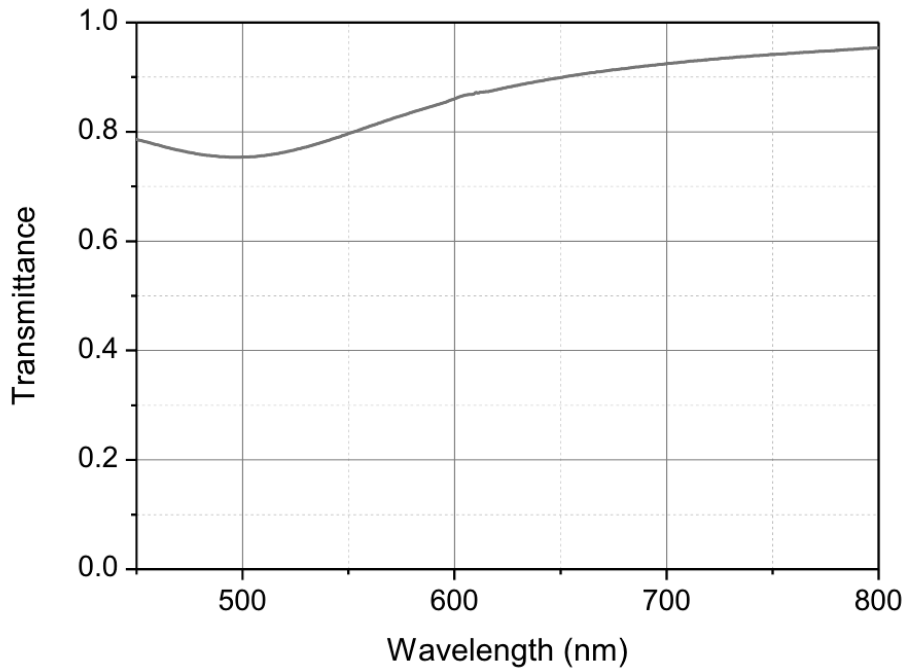

Figure 4.2 Transmittance spectrum of interconnection layer of tandem device composed of 10 nm BCP:Ag / 0.5 nm Ag island / 10 nm HAT-CN.

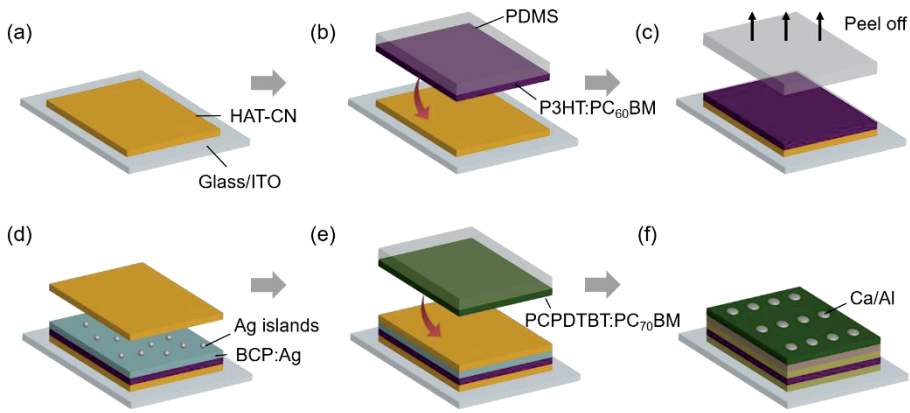

Figure 4.3 (a) Deposition of a HAT-CN layer on a UV-ozone treated ITO substrate. (b) Transfer of a P3HT:$PC_{60}BM$ film from a stamp to the HAT-CN layer. (c) Peeling off the stamp from the substrate. (d) Deposition of an ICL onto the bottom subcell using thermal evaporation in a vacuum. (e) Transfer of a PCPDTBT:$PC_{70}BM$ layer onto the ICL. (f) Deposition of the top electrodes.

4.3 *J–V* characteristics of polymer tandem solar cells by varying the thickness of the interconnection layer

To maximize the performance of the polymer tandem solar cell, a series of devices with varying thicknesses of the BCP:Ag ($t_{BCP:Ag}$) and Ag islands (t_{Ag}) layers of the ICL were fabricated. Fig. 4.4a shows the current density versus voltage (*J–V*) characteristics of the tandem device with varying $t_{BCP:Ag}$ and with t_{Ag} and the thickness of the HAT-CN layer fixed at 0.5 nm and 10 nm, respectively, measured under simulated 1 sun AM1.5G illumination. The photovoltaic parameters of the devices are summarized in Table 3. When the BCP:Ag layer was omitted ($t_{BCP:Ag}$ = 0 nm, red), the addition of the subcell V_{OC} values, expected for a series connected tandem device, did not occur, leading to V_{OC} of only 0.62 V. With a J_{SC} of 6.18 mA cm^{-2} and FF of 0.39, this device has a power-conversion efficiency (PCE) of 1.49%, the lowest among the six devices that were fabricated. In contrast, insertion of a BCP:Ag layer that was only 5 nm thick made this device ($t_{BCP:Ag}$ = 5 nm, blue) operate as a tandem cell: the value of V_{OC} abruptly increased to 1.09 V, similar to the sum of the subcell V_{OC} values. The values of J_{SC} (7.34 mA cm^{-2}) and FF (0.53) were also improved, and consequently a much higher PCE (4.24%) was achieved. When $t_{BCP:Ag}$ was 10 nm (black), the device showed better performance, exhibiting V_{OC} = 1.20 V, J_{SC} = 7.24 mA cm^{-2} , FF = 0.60, and

PCE = 5.21%. As $t_{BCP:Ag}$ was increased beyond 10 nm, the PCE became progressively smaller, primarily because of the decreased J_{SC} and FF: the device with $t_{BCP:Ag}$ = 15 nm (green) exhibited J_{SC} = 5.20 mA cm^{-2} , FF = 0.48, and PCE = 3.00%, whereas the PCE of the device with $t_{BCP:Ag}$ = 30 nm (brown) was 2.08%, with an s-kink in the *J–V* curve.

Next, the effect of t_{Ag} on device performance was investigated by fabricating tandem cells with t_{Ag} = 0, 0.5, and 2 nm while setting both $t_{BCP:Ag}$ and the HAT-CN thickness at 10 nm. The *J–V* characteristics of the three devices shown in Fig. 4.4b show that the performance was maximized at t_{Ag} = 0.5 nm, with its PCE higher by 24% and 56% compared to the PCEs of the devices with t_{Ag} = 0 and 2 nm, respectively. The values of J_{SC}, V_{OC}, and FF of the optimized tandem cell (with t_{Ag} of 0.5 nm) were larger than the corresponding values of the other two cells, and the tandem cell with t_{Ag} = 2 nm exhibited J_{SC} = 5.47 mA cm^{-2} that was smaller by 20% and 24%, respectively, than that of the cells with t_{Ag} = 0 and 0.5 nm (Table 4). Additional information, such as the external quantum efficiency (Fig. 4.5) and the ambient stability (Fig. 4.6) of the optimized tandem cell, and the device-to-device variations of the *J–V* characteristics and the photovoltaic parameters of the tandem cells shown in Fig. 4.4b is shown in Fig. 4.7. Figure 4.4c compares the photovoltaic parameters of the six tandem devices having different ($t_{BCP:Ag}$,

t_{Ag}), demonstrating that the performance of the polymer tandem solar cell was altered even with very small changes in $t_{BCP:Ag}$ and/or t_{Ag}. Thorough optimization, therefore, requires a precise control of the layer thicknesses, which can be routinely achieved using vacuum thermal evaporation.

Figure 4.4d compares the *J–V* characteristics of the optimized tandem device ($t_{BCP:Ag}$ = 10 nm, t_{Ag} = 0.5 nm) with the characteristics of the two single junction devices forming the tandem cell. The structures of the single junction devices were glass/ 185 nm ITO/10 nm HAT-CN/ ~ 200 nm P3HT:$PC_{60}BM$/10 nm BCP:Ag/100 nm Ag (blue), and glass/185 nm ITO/10 nm HAT-CN/ ~ 90 nm PCPDTBT:$PC_{70}BM$/20 nm Ca/100 nm Al (red), where the P3HT:$PC_{60}BM$ and PCPDTBT:$PC_{70}BM$ layers were transfer printed on the HAT-CN layers, as in the fabrication of the tandem device. The photovoltaic parameters of the single junction devices, summarized in the inset of Fig. 4.4d, were in good agreement with those of the corresponding spin-coated devices using PEDOT:PSS in place of HAT-CN [9,25], confirming that the P3HT:$PC_{60}BM$–HAT-CN and PCPDTBT:$PC_{70}BM$–HAT-CN interfaces formed using transfer printing were sufficiently intimate to allow for efficient charge transport. It is worth noting that the tandem cell (black), having FF = 0.60 and V_{OC}= 1.20 V that were almost identical to the FFs of the single junction cells and the sum of the V_{OC} values of the single junction cells, respectively, exhibited a *J–V*

characteristic that was expected when the two subcells were connected with an optimal ICL ensuring efficient transport and recombination of photogenerated electrons and holes. This result demonstrated that the dry thin-film transfer technique allows the exploitation, for polymer tandem solar cells, of the advantage of an ICL composed of small molecules and metals that can be thermally evaporated – full optimization of the ICL performance by precise tuning of layer thicknesses.

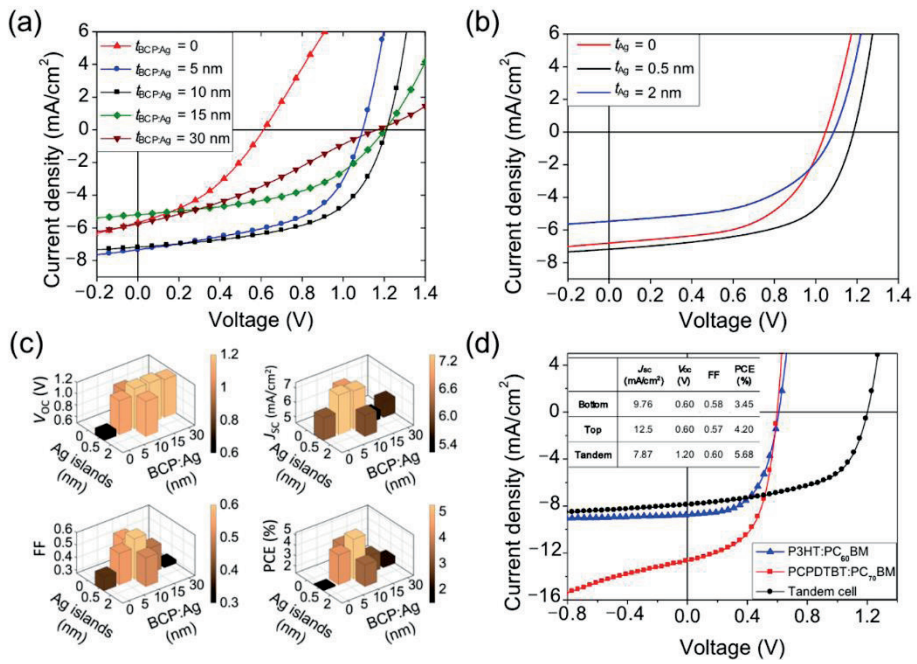

Figure 4.4 Photovoltaic characteristics of polymer tandem solar cells using an ICL with varying thicknesses of BCP:Ag layer and Ag islands ($t_{BCP:Ag}$ and t_{Ag}, respectively). (a) *J*–*V* characteristics of the tandem cells with t_{Ag} = 0.5 nm and different $t_{BCP:Ag}$ values. (b) *J*–*V* characteristics of the tandem cells with $t_{BCP:Ag}$ = 10 nm and different t_{Ag} values. (c) Photovoltaic parameters of the tandem cells as functions of $t_{BCP:Ag}$ and t_{Ag}. (d) *J*–*V* characteristics of the tandem device with $t_{BCP:Ag}$ = 10 nm and t_{Ag} = 0.5 nm, compared with the characteristics of the single junction devices. Inset: photovoltaic parameters of the three devices.

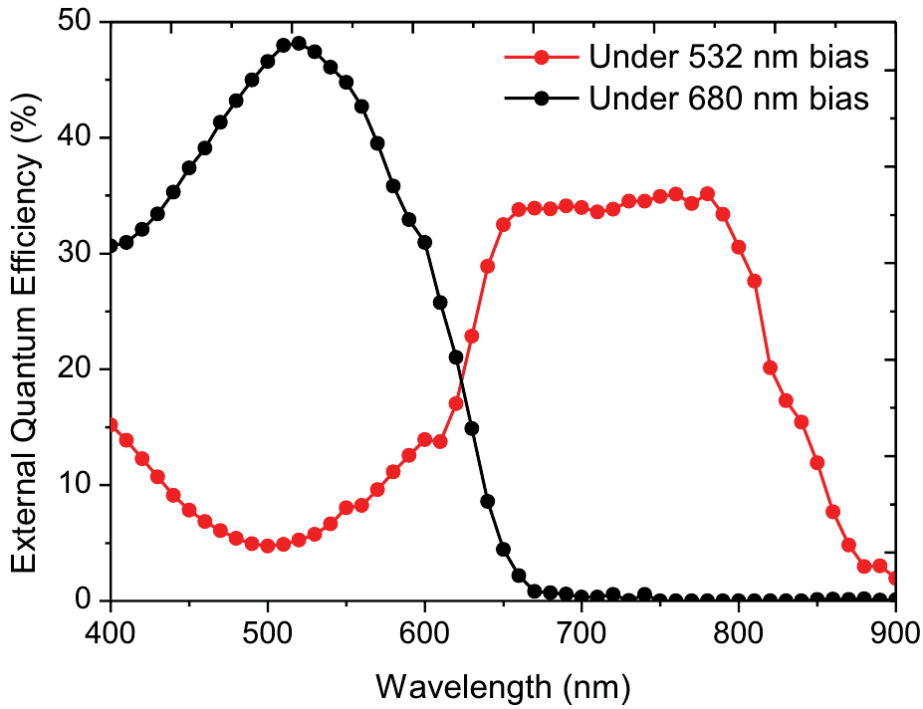

Figure 4.5 External quantum efficiency (EQE) spectra of the tandem device with $t_{BCP:Ag}$ = 10 nm and t_{Ag} = 0.5 nm measured under light biases at 532 nm (red) and 680 nm (black) show a qualitative agreement with the calculated absorption spectra of the subcells shown in Fig. 4.1b. The EQE measurements were performed by following a method described elsewhere [27]. A monochromatic light generated using a laser-driven light source (EQ-99, Energetiq) and a monochromator (Monora 200, Dongwoo Optron) was modulated by a chopper at a frequency of ~400 Hz before irradiating the device, and the resulting photocurrent was measured using a current amplifier (SR570, Stanford Research) and a lock-in amplifier (SR830, Stanford Research).

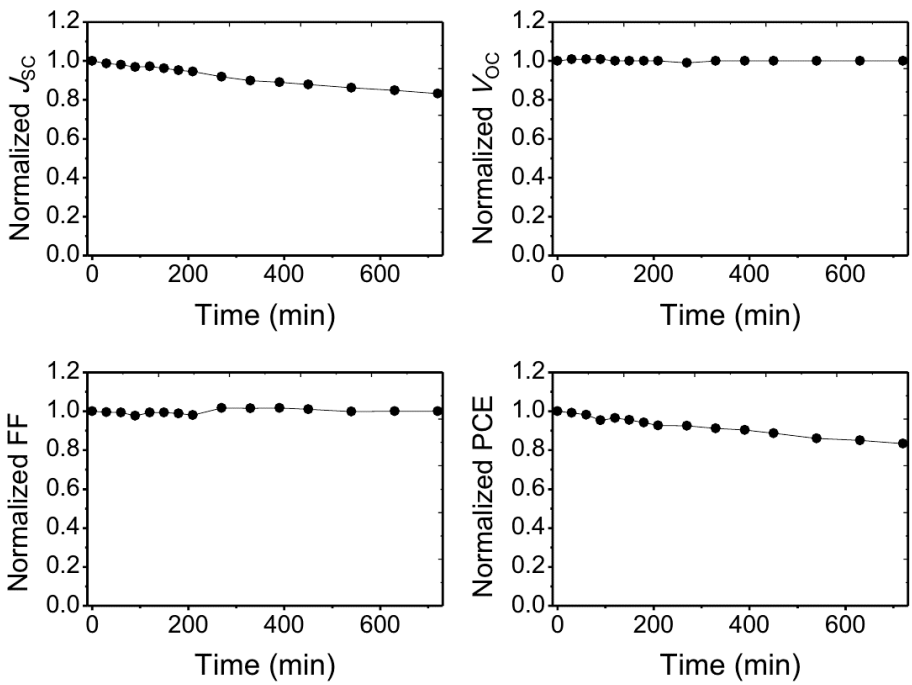

Figure 4.6 Photovoltaic parameters extracted from intermittently measured *J*–*V* characteristics of the optimized tandem cell. The measurement was performed without encapsulation in ambient at 50 % relative humidity.

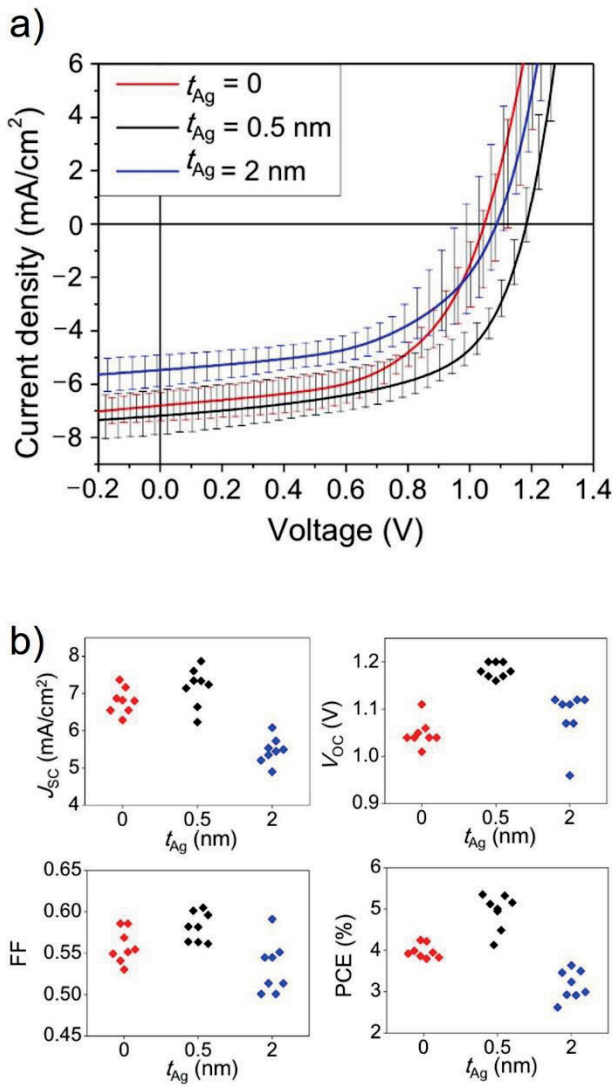

Figure 4.7 (a) Device-to-device variations of the *J–V* characteristics of the tandem cells shown in Fig. 4.4b. Top and bottom of errors bars correspond to maximum and minimum values obtained from eight devices for each tandem cell. (b) The photovoltaic parameters of all twenty-four devices, eight for each tandem cell.

Table 3 Photovoltaic parameters of polymer tandem solar cells with t_{Ag} = 0.5 nm and different $t_{BCP:Ag}$ values.

	J_{SC} (mA cm^{-2})	V_{OC} (V)	FF	PCE (%)
Without BCP:Ag	6.18	0.62	0.39	1.49
BCP:Ag (5 nm)	7.34	1.09	0.53	4.24
BCP:Ag (10 nm)	7.24	1.20	0.60	5.21
BCP:Ag (15 nm)	5.20	1.20	0.48	3.00
BCP:Ag (30 nm)	5.74	1.16	0.31	2.08

Table 4 Photovoltaic parameters of polymer tandem solar cells with $t_{BCP:Ag}$ = 10 nm and different t_{Ag} values.

	J_{SC}[a] (mA cm^{-2})	V_{OC}[a] (V)	FF[a]	PCE[a] (%)
Without Ag islands	6.80	1.05	0.56	3.98
0.5 nm Ag islands	7.18	1.18	0.58	4.94
2 nm Ag islands	5.47	1.09	0.53	3.16

[a]Averaged over eight devices

4.4 Qualitative explanation of the dependency of tandem cell performance on $t_{BCP:Ag}$ and t_{Ag}

The dependence of the tandem cell performance on $t_{BCP:Ag}$ and t_{Ag} can be qualitatively explained by considering the operational mechanism of the BCP:Ag/Ag islands/HAT-CN ICL layer that was hypothesized. It was first noted that a hole generated in PCPDTBT by dissociation of an exciton in the top active layer cannot be transported to the HAT-CN layer because of the deep highest occupied molecular orbital (HOMO) level of HAT-CN. Therefore, an electron photogenerated in the bottom cell must be transported to the HAT-CN so that the recombination of an electron and a hole photogenerated in the bottom and top active layers, respectively, occurs at the HAT-CN– PCPDTBT interface, as marked by a wavy red arrow in Fig. 4.8a, respectively. This required transport of electrons from the $PC_{60}BM$ to the HAT-CN was greatly facilitated by the insertion of the BCP:Ag and Ag island layers as follows: electrons in the $PC_{60}BM$ layer were transported through the gap states present in the BCP:Ag [24], which were then injected into the HAT-CN either directly or *via* the Ag islands, as marked by arrow (i) or (ii) in Fig. 4.8a, respectively. The Ag islands further enhanced the electron transport through the gap states in the BCP:Ag by increasing the number of unoccupied gap states in the BCP:Ag by extracting some electrons from the BCP:Ag.

The tandem device using the optimized ICL (black, Fig. 4.4a) exhibited the best performance because the electrons and holes generated in the bottom and top subcells, respectively, readily recombine with each other through the process described previously. However, when the BCP:Ag was omitted (Fig. 4.8b), it became difficult for the photogenerated electrons in the $PC_{60}BM$ to be transported to the HAT-CN *via* the Ag islands, which was in agreement with an abrupt degradation of the performance of the P3HT:$PC_{60}BM$ single junction device upon omission of the BCP:Ag layer, as shown in Fig. 4.9.

The resulting accumulation of electrons increases the likelihood of bimolecular recombination, limiting electron generation in the bottom active layer. As a result, electrons in the HAT-CN that are to recombine with holes in the PCPDTBT were more likely to be injected from the HOMO of P3HT, directly from the P3HT or via the Ag islands, as shown by arrows (iii) or (iv), respectively, in Fig. 4b. At the same time, photogenerated holes in the PCPDTBT were collected at the ITO electrode *via* the hole current flowing through the P3HT, as marked by a red horizontal arrow in Fig. 4.8b. Consequently, the device with $t_{BCP:Ag}$ = 0 nm and t_{Ag} = 0.5 nm (red, Fig. 4.4a) did not operate as a tandem device, resulting in a small V_{OC} comparable to that of the PCPDTBT:$PC_{70}BM$ single junction device. In the device with $t_{BCP:Ag}$ = 5 nm and t_{Ag} = 0.5 nm, it was likely that P3HT was in direct contact with HAT-

CN in some regions because of the diffusion of P3HT [24], which caused a V_{OC} loss by direct extraction of holes generated in the top subcell through the P3HT (blue, Fig. 4.4a). The decrease in FF observed when $t_{BCP:Ag}$ was increased beyond the optimal value of 10 nm (green and brown, Fig. 4.4a) suggested that electron transport through the BCP:Ag became less efficient. This was likely to have occurred because the number of unoccupied gap states in the BCP:Ag became insufficient with increasing $t_{BCP:Ag}$ because of the limited amount of electrons that the Ag island layer with t_{Ag} = 0.5 nm can extract. In fact, an observation that the FF of the tandem cell with $t_{BCP:Ag}$ = 30 nm was increased to 0.59 when t_{Ag} was increased to 5 nm was in agreement with this hypothesis (Fig. 4.10). The slight decreases in FF and V_{OC} of the device with $t_{BCP:Ag}$ = 10 nm and without Ag islands (red, Fig. 4.4b) compared with those of the optimized device can also be explained by the decreased number of unoccupied gap states in the BCP:Ag. It was likely that the decrease in J_{SC} observed when t_{Ag} was increased to 2 nm was because of increased parasitic absorption in the Ag islands (blue, Fig. 4.4b).

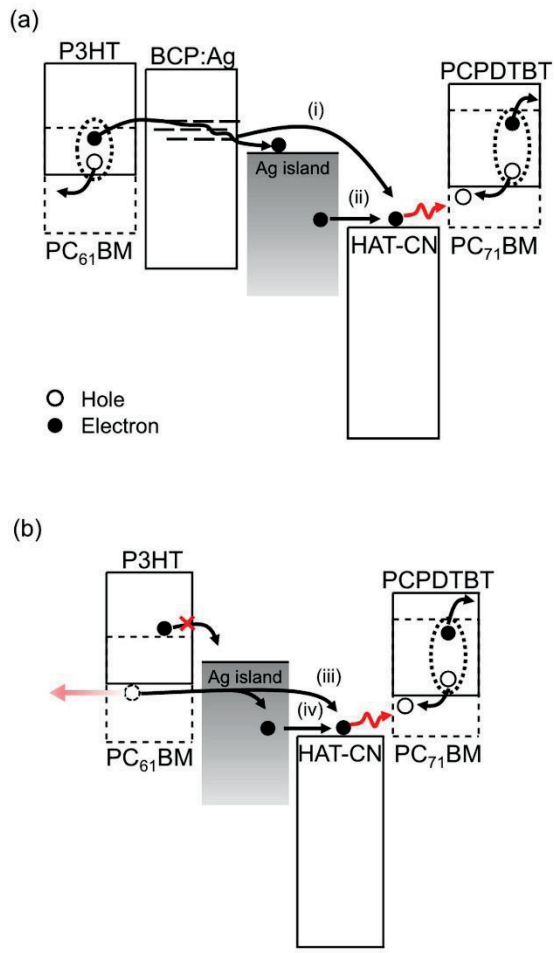

Figure 4.8 (a) Schematic illustration of the operational mechanism of the tandem device with BCP:Ag/Ag islands/HAT-CN ICL. (b) Schematic illustration of the origin of V_{OC} loss observed when the BCP:Ag layer in the ICL is omitted.

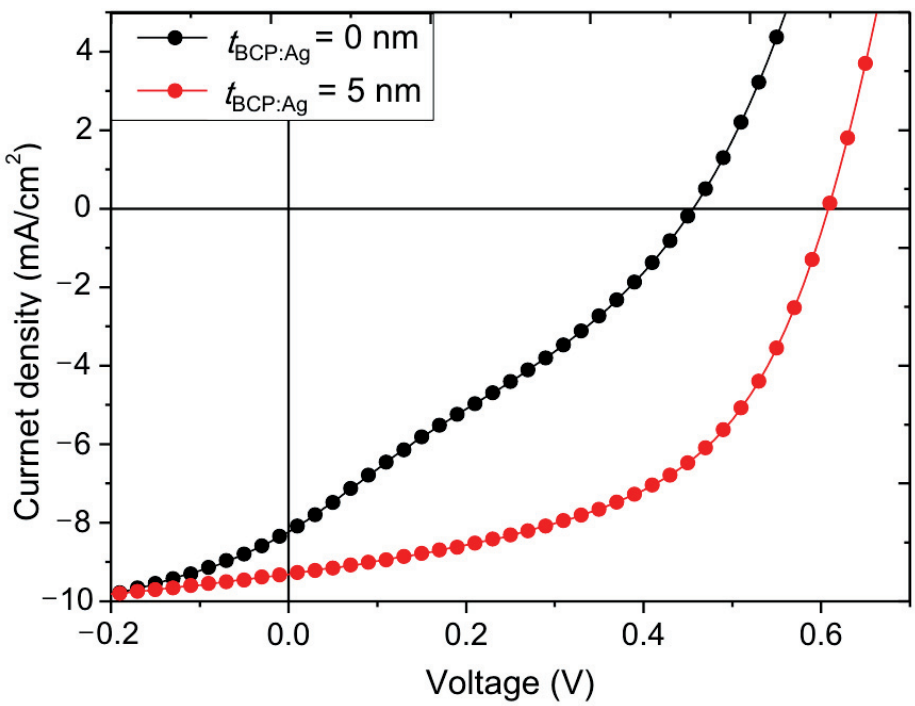

Figure 4.9 *J–V* characteristics of P3HT:$PC_{60}BM$ single-junction devices, without a BCP:Ag layer (black) and with a 5-nm-thick BCP:Ag layer (red).

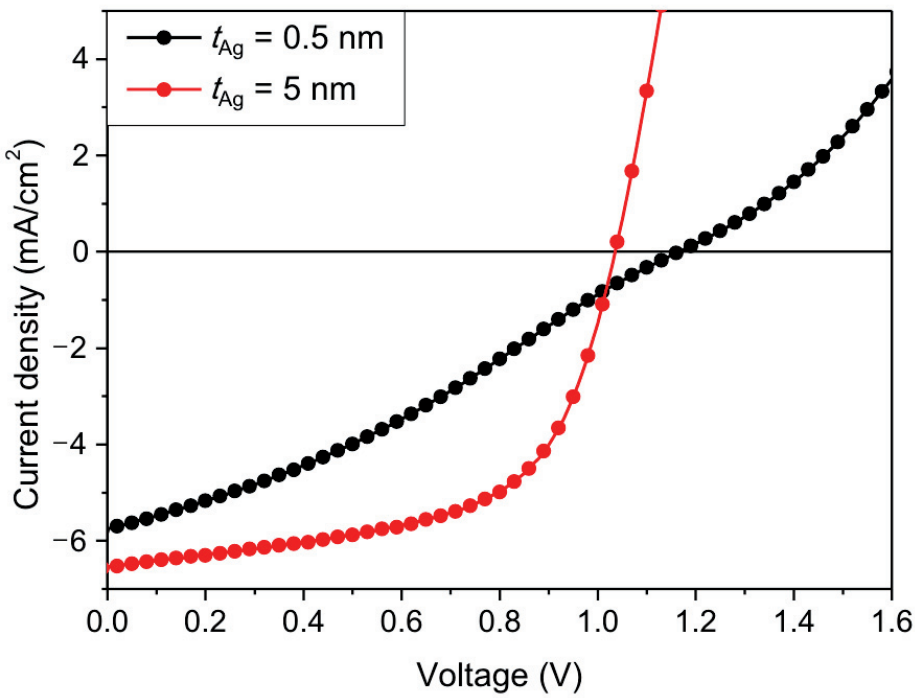

Figure 4.10 *J–V* characteristics of polymer tandem devices with ($t_{BCP:Ag}$, t_{Ag}) = (30 nm, 0.5 nm) (black) and ($t_{BCP:Ag}$, t_{Ag}) = (30 nm, 5 nm) (red), respectively.

4.5 Conclusion

By depositing the active layer of the top subcell using the thin-film transfer technique, an ICL composed of vacuum deposited BCP:Ag/Ag islands/HAT-CN that would otherwise be damaged by a solvent used for the active layer became applicable to polymer tandem solar cells based on the P3HT:$PC_{60}BM$ and PCPDTBT:$PC_{70}BM$ layers. The thicknesses of the BCP:Ag and Ag island layers were precisely controlled to facilitate the transport of electrons generated in the bottom subcell, leading to their efficient recombination with holes generated in the top subcell. As a result, the tandem device featuring the optimized ICL exhibited a V_{OC} of 1.20 V, which was equal to the sum of the V_{OC} values of the two subcells, with its FF (0.60) almost identical to the FFs of the subcells. This work shows that the thin-film transfer technique, together with the advantageous attributes of vacuum thermal evaporation, may contribute to the future development of efficient polymer tandem solar cells by offering a large degree of freedom in selection of materials and structures for ICLs.

4.6 References

[1] H. Hoppe, N. S. Sariciftci, Organic solar cells: An overview, J. Mater. Res., 19 (2011) 1924–1945.

[2] H. Spanggaard, F. C. Krebs, A brief history of the development of organic and polymeric photovoltaics, Sol. Energy Mater. Sol. Cells, 83 (2004) 125–146.

[3] J. You, L. Dou, K. Yoshimura, T. Kato, K. Ohya, T. Moriarty, K. Emery, C. C. Chen, J. Gao, G. Li, Y. Yang, A polymer tandem solar cell with 10.6% power conversion efficiency, Nat. Commun., 4 (2013) 1446.

[4] S. Sista, Z. Hong, L.-M. Chen, Y. Yang, Tandem polymer photovoltaic cells—current status, challenges and future outlook, Energy Environ. Sci., 4 (2011) 1606–1620.

[5] T. Aernouts, T. Aleksandrov, C. Girotto, J. Genoe, J. Poortmans, Polymer based organic solar cells using ink-jet printed active layers, Appl. Phys. Lett., 92 (2008) 033306-1−033306-3.

[6] C. Girotto, B. P. Rand, J. Genoe, P. Heremans, Exploring spray coating as a deposition technique for the fabrication of solution-processed solar cells, Sol. Energy Mater. Sol. Cells, 93 (2009) 454–458.

[7] J. Gilot, M. M. Wienk, R. A. J. Janssen, Double and triple junction polymer solar cells processed from solution, Appl. Phys. Lett., 90 (2007) 143512-1−

143512-3.

[8] S. Kouijzer, S. Esiner, C. H. Frijters, M. Turbiez, M. M. Wienk, R. A. J. Janssen, Efficient Inverted Tandem Polymer Solar Cells with a Solution-Processed Recombination Layer, Adv. Energy Mater., 2 (2012) 945–949.

[9] J. Y. Kim, K. Lee, N. E. Coates, D. Moses, T. Q. Nguyen, M. Dante, A. J. Heeger, Efficient tandem polymer solar cells fabricated by all-solution processing, Science, 317 (2007) 222–225.

[10] M. Girtan, M. Rusu, Role of ITO and PEDOT:PSS in stability/degradation of polymer:fullerene bulk heterojunctions solar cells, Sol. Energy Mater. Sol. Cells, 94 (2010) 446–450.

[11] C.-H. Chou, W. L. Kwan, Z. Hong, L.-M. Chen and Y. Yang, A metal-oxide interconnection layer for polymer tandem solar cells with an inverted architecture, Adv. Mater., 23 (2011) 1282–1286.

[12] K. X. Steirer, P. F. Ndione, N. E. Widjonarko, M. T. Lloyd, J. Meyer, E. L. Ratcliff, A. Kahn, N. R. Armstrong, C. J. Curtis, D. S. Ginley, J. J. Berry, D. C. Olson, Enhanced Efficiency in Plastic Solar Cells via Energy Matched Solution Processed NiO_x Interlayers, Adv. Energy Mater., 1 (2011) 813–820.

[13] J. R. Manders, S.-W. Tsang, M. J. Hartel, T.-H. Lai, S. Chen, C. M. Amb, J. R. Reynolds, F. So, Solution-Processed Nickel Oxide Hole Transport Layers in High Efficiency Polymer Photovoltaic Cells, Adv. Funct. Mater., 23 (2013)

2993–3001.

[14] V. Shrotriya, G. Li, Y. Yao, C.-W. Chu, Y. Yang, Appl. Phys. Lett., 2006, 88, 073508-1–073508-3.

[15] S. Han, W. S. Shin, M. Seo, D. Gupta, S.-J. Moon, S. Yoo, Improving performance of organic solar cells using amorphous tungsten oxides as an interfacial buffer layer on transparent anodes. Org. Electron., 10 (2009) 791–797.

[16] J. Sakai, K. Kawano, T. Yamanari, T. Taima, Y. Yoshida, A. Fujii, M. Ozaki, Efficient organic photovoltaic tandem cells with novel transparent conductive oxide interlayer and poly (3-hexylthiophene): Fullerene active layers, Sol. Energy Mater. Sol. Cells, 94 (2010) 376–380.

[17] R. Schueppel, R. Timmreck, N. Allinger, T. Mueller, M. Furno, C. Uhrich, K. Leo and M. Riede, Controlled current matching in small molecule organic tandem solar cells using doped spacer layers, J. Appl. Phys., 107 (2010) 044503-1–044503-6.

[18] T.-Y. Li, T. Meyer, Z. Ma, J. Benduhn, C. Körner, O. Zeika, K. Vandewal, K. Leo, Small Molecule Near-Infrared Boron Dipyrromethene Donors for Organic Tandem Solar Cells, J. Am. Chem. Soc., 139 (2017) 13636–13639.

[19] H.-S. Shim, J.-H. Chang, C.-I. Wu and J.-J. Kim, Effect of different p-dopants in an interconnection unit on the performance of tandem organic solar

cells, Org. Electron., 15 (2014) 1805–1809.

[20] E. Lee, J. Kim, C. Kim, Polymer tandem photovoltaic cells with molecularly intimate interfaces achieved by a thin-film transfer technique, Sol. Energy Mater. Sol. Cells, 105 (2012) 1–5.

[21] Y. Ka, H. Hwang, C. Kim, Hybrid organic tandem solar cell comprising small-molecule bottom and polymer:fullerene top subcells fabricated by thin-film transfer, Sci. Rep., 7 (2017) 1942-1−1942-8.

[22] L. A. A. Pettersson, L. S. Roman and O. Inganäs, Modeling photocurrent action spectra of photovoltaic devices based on organic thin films, J. Appl. Phys., 86 (1999) 487–496.

[23] H. Kim, J.-H Kim, J.-K Kim, J. Seo, Y. Park, Interface electronic structure of a strongly electron withdrawing molecule on an indium-tin-oxide surface, J. Korean Phys. Soc., 59 (2011) 3060–3063.

[24] G. H. Jung and J.-L. Lee, Origin of gap states in the electron transport layer of organic solar cells, J. Mater. Chem. A, 1 (2013) 3034–3039.

[25] G. Li, Y. Yao, H. Yang, V. Shrotriya, G. Yang, Y. Yang, “Solvent annealing” effect in polymer solar cells based on poly(3-hexylthiophene) and methanofullerenes, Adv. Funct. Mater., 17 (2007) 1636–1644.

[26] A. Zusan, B. Gieseking, M. Zerson, V. Dyakonov, R. Magerle, C. Deibel, The effect of diiodooctane on the charge carrier generation in organic solar

cells based on the copolymer PBDTTT-C. Sci. Rep., 5 (2015) 8286-1−8286-8.

[27] J. Gilot, M. M. Wienk, R. A. J. Janssen, Measuring the external quantum efficiency of two-terminal polymer tandem solar cells, Adv. Funct. Mater., 20 (2010) 3904–3911.

Chapter 5 Conclusion

In summary, I have developed a low-temperature solution process for ZnO thin-film deposition, which is an electron transport layer material. In addition, by developing a thin-film transfer technique of polymer:fullerene layer using the PDMS stamp, it is possible to overcome the limitation of conventional process and realize high efficiency organic tandem solar cells. First, ZnO thin-film deposition method using ammine-hydroxo zinc complex based on low-temperature solution process was applied to inverted polymer solar cell to enable fabrication of devices at low process temperature. Thus, a device applicable to plastic substrates such as PET and PEN was realized. The device has the same performance as the device fabricated at a temperature of 100 ºC or higher even at a low-process temperature of 80 ºC. The influence of the annealing temperature of the ZnO thin-film on the characteristics of the thin-film is analyzed by XPS, UPS, GI-WAXS, and optical transmittance.

Next, I developed a thin-film transfer technique of polymer:fullerene layer and overcome the process limit of the organic tandem solar cell (hybrid & polymer) containing polymer:fullerene layer, which forms a thin-film through the solution process. Through this, I successfully applied the device structure and new ICL, which could not be realized by the conventional process method. Using this, I fabricated a small-molecule bottom and polymer

top hybrid organic tandem solar cell and enabled the efficient organic tandem device considering only the complementary absorption spectrum. As a result, the highest efficiency of organic hybrid tandem solar cells that has been reported is 6.5%.

Finally, a small-molecule-based ICL formed through a vacuum thermal deposition process was applied to a polymer tandem solar cell, in which only a limited range of ICLs (PEDOT:PSS / metal oxide) could be applied using thin-film transfer. This has drastically improved the flexibility of selecting materials and designing of ICLs for polymer tandem solar cells. By applying the ICL formed by the vacuum thermal deposition process to the polymer tandem device, it was possible to form an ideal ICL that perfectly connects each subcell without voltage loss through doping and fine-tuning the thickness.

These results are noteworthy studies that could speed up the implementation of high efficiency organic solar cells by overcoming the process limitations of organic solar cell fabrication and increasing the degree of freedom in terms of device design. Through the deposition of the electron transport layer through the low-temperature solution process, it is expected that a flexible device can be realized. Furthermore, the optimization process of the organic tandem solar cell can be facilitated through the thin-film transfer technique, thereby promoting the commercialization of the organic solar cell.

I believe that the process limitations for the fabrication of high efficiency tandem devices can be solved by the transfer process developed in this study. In other words, it can be said that the limit of the arrangement of the materials is almost overcome. The direction of the research to be performed additionally for the realization of the high efficiency organic tandem solar cells can be summarized as follows. Currently used organic light absorbing materials have a light absorption loss due to the overlapping use of similar types of fullerene materials. At this time, since the overlap in the short wavelength region partially occurs even in the case of the donor material, the charge is not sufficiently generated. In order to overcome these limitations, it is necessary to develop donor materials that only absorb the long wavelength region and/or to develop non-fullerene acceptor materials to avoid overlap of short wavelength photon absorption. It is also required to develop an ICL composed of a material having a high transmittance in the absorption region of each subcell in order to increase the absorption of photons lost by the absorption of the ICL, as shown in the hybrid organic tandem solar cells of chapter 3 (Fig. 5.1).

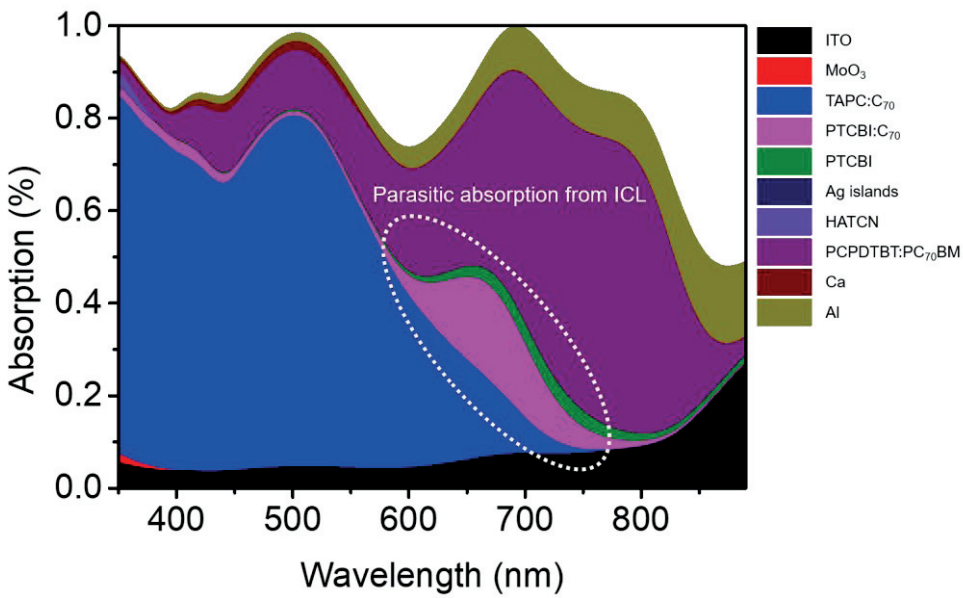

Figure 5.1 Absorption of each layer of hybrid organic tandem solar cell in chapter 3

요약 (국 문 초 록)

유기 태양전지의 상용화를 위해 연구진들이 가장 관심을 갖는 분야는 플렉서블 소자 구현과 실리콘 기반의 태양전지에 버금갈 수 있는 고효율의 소자 구현이라고 이야기 할 수 있다.

플렉서블 태양전지와 고효율 유기 태양전지의 구현을 위해서는 이를 가능하게 하는 자유로운 소자 디자인이 동반되어야 한다. 소자 디자인의 자유도를 저해하는 문제는 주로 용액 공정을 통해 박막을 형성하는 과정에서 발생하며, 이러한 문제는 크게 다음과 같은 두가지로 정리할 수 있다. 첫째, 용액 공정을 통해 형성한 박막의 고온 열처리 과정에서 발생하는 하부 유기물 및 플라스틱 기판의 손상 문제. 둘째, 박막 형성 과정에서 사용되는 유기 용매에 의한 하부 유기물 층의 손상 문제. 따라서, 저온 용액 공정의 개발과 유기 용매에 의한 하부 유기물 층의 손상을 방지할 수 있는 박막 형성 기술의 개발은 소자 디자인 자유도를 높임으로써 상용화가 가능한 고효율 유기 태양전지 제작을 위해 반드시 필요한 요소라고 할 수 있다.

본 학위논문에서는 유기 태양전지 제작을 위한 일반적인 공정 방법이 극복하지 못한 문제를 새로운 공정 방법을 개발함으로써 유기 태양전지의 디자인 자유도 향상을 가능하게 한 연구 결과에 대해 설명한다. 먼저, 플렉서블 소자 구현을 위한 저온 용액 공정

이 가능한 전자 수송층 형성법인 aqueous ammine-hydroxo법을 사용한 ZnO 박막 형성법에 대해 소개하고, 이를 inverted polymer solar cell에 적용하여 80 ºC의 낮은 공정온도에서도 높은 성능을 보이는 소자 구현이 가능함을 보였다. 또한, ZnO 박막 형성과정에서 annealing 온도가 박막의 특성에 미치는 영향을 XPS, UPS, GI-WAXS, Transmittance 측정 등을 통해 확인 하였다. 다음으로 PDMS stamp를 사용한 고분자 박막 전사 공정을 개발하여 유기 탠덤 태양전지 제작에 적용함으로써, 유기 용매에 의한 유기물 층의 손상 문제를 극복한 결과, 하이브리드 유기 탠덤 태양전지의 단분자와 고분자 광흡수층 배치의 자유도를 높여 상보적인 광 흡수 스펙트럼만을 고려한 효율적인 흡수층의 배치를 가능하였다. 그 결과 지금까지 보고된 하이브리드 유기 탠덤 태양전지 중 가장 높은 전력변환 효율을 달성하였다. 마지막으로 박막 전사 공정을 고분자 탠덤 태양전지에 적용하였다. 이를 통해 기존에 PEDOT:PSS와 metal oxide의 조합으로 구성된 제한된 종류의 중간 전극 만이 사용되었던 기존 연구의 한계를 극복하고 진공 열증착 공정을 통해 형성한 단분자 기반의 중간 전극을 고분자 탠덤 태양전지에 성공적으로 적용할 수 있음을 보였다. 이 연구 결과를 기반으로 상·하부 subcell을 전기적·광학적 손실 없이 연결하는 탠덤 태양전지의 중간 전극 개발을 위한 물질 선택의 자유도를 획기적으로 향상시켰다.

.....

주 요 어: 유기전자소자, 태양 전지, 전사, 박막, 단분자,
고분자, 중간 전극

학 번: 2011-22751